

## CANCER

# Caspase-1–dependent pyroptosis converts $\alpha$ SMA<sup>+</sup> CAFs into collagen-III<sup>high</sup> iCAF to fuel chemoresistant cancer stem cells

Hongbo Gao<sup>1\*</sup>, Stephen Q. R. Wong<sup>1</sup>, Ethan Subel<sup>1</sup>, Yung Hsing Huang<sup>1</sup>, Yu-Cheng Lee<sup>2</sup>, Kazukuni Hayashi<sup>3</sup>, Mark Ellie Alonzo<sup>1,4</sup>, Mustafa Karabiccici<sup>5</sup>, Xen Ping Hoi<sup>1,4</sup>, Armine Kasabyan<sup>1</sup>, Qianxing Mo<sup>6</sup>, Zachary Melchiodi<sup>1†</sup>, Ziad El-Zaatari<sup>1</sup>, Steven Shen<sup>1</sup>, Raj Satkunasivam<sup>1</sup>, Fotis Nikolos<sup>1</sup>, Keith Syson Chan<sup>1\*</sup>

The impact of chemotherapy-induced tumor cell pyroptosis on fibroblasts, a key stromal cell type within the tumor microenvironment (TME), remains unexplored. Here, we report morphologically and molecularly distinct subtypes of cancer-associated fibroblasts (CAFs) in bladder cancer, including  $\alpha$ SMA<sup>+</sup>IL-6<sup>-</sup> myofibroblastic CAFs (myCAFs),  $\alpha$ SMA<sup>-</sup>IL-6<sup>+</sup> inflammatory CAFs (iCAFs), and hybrid i/myCAFs. Caspase-1–dependent tumor pyroptosis releases several inflammatory chemokines, converting  $\alpha$ SMA<sup>+</sup> CAF into iCAF in a CCR6-dependent manner. This is clinically relevant, as a fibroblast gene signature driven by iCAF markers and collagen type III is enriched in patients with chemoresistant bladder cancer after neoadjuvant chemotherapy. Contrary to the current notion, iCAFs, rather than myCAFs, produce collagen III in response to chemotherapy, supporting the expansion of cancer stem cells (CSCs). Thus, tumor cell pyroptosis initiates an iCAF-CSC feedforward loop that drives chemoresistance, indicating that inflammatory cell death is not universally beneficial to anticancer therapy, depending on the target cell type.

## INTRODUCTION

Canonical pyroptosis, also known as “inflammatory fiery death,” is a programmed lytic cell death that depends on active caspase-1 (Casp1) to cleave its major substrate, gasdermin D (GSDMD) (1–5). The N terminus of GSDMD forms pores on the plasma membrane of pyroptotic cells for extracellular release of their intracellular contents (3, 5, 6). This canonical pyroptotic pathway is extensively investigated in macrophages, and its effects on immune cells in the tumor microenvironment (TME) to exert antitumoral activities are well documented (7). However, whether cancer cells are prone to canonical pyroptotic cell death, or whether chemotherapy-induced tumor pyroptosis influences fibroblasts, a major stromal cell type within the TME, remains unexplored.

During wound healing, tissue resident quiescent fibroblasts become activated to repair damaged parenchymal cells and deposit collagens to induce wound closure (8). In the cancer context, cancer-associated fibroblasts (CAFs) reprogrammed by tumor cells retain an activated state (9). However, the mechanisms by which CAFs remain continuously activated are incompletely understood. CAFs are a key component in stromal TME and are increasingly acknowledged as a co-contributor to tumorigenesis (10, 11), chemoresistance (12), and metastasis (13, 14). To date, most functional studies predominantly considered CAFs as a homogeneous population of myofibroblasts, which are often characterized as  $\alpha$ -smooth muscle

actin high ( $\alpha$ SMA<sup>high</sup>) CAFs (15). Recent single-cell RNA sequencing (scRNA-seq) studies have revealed transcriptionally distinct CAF subtypes among many solid cancers (16–20), which were not captured by previous functional studies. In pancreatic cancer,  $\alpha$ SMA<sup>+/high</sup> fibroblasts, enriched with myofibroblast gene signatures and matrix-rich gene expression, were defined as myofibroblastic CAFs (myCAFs;  $\alpha$ SMA<sup>+/high</sup>). Alternatively, interleukin-6 high (IL-6<sup>high</sup>) CAFs, which lack *ACTA2* ( $\alpha$ SMA<sup>-</sup>), were classified as inflammatory CAFs (iCAFs;  $\alpha$ SMA<sup>-</sup>IL-6<sup>high</sup>) (21, 22).  $\alpha$ SMA<sup>+/high</sup> CAFs have also been reported to coexpress IL-6 ( $\alpha$ SMA<sup>high</sup>IL-6<sup>high</sup>), contributing to chemoresistance (23). These observations suggest that additional CAF subtypes may exist beyond the traditionally defined pure myCAFs ( $\alpha$ SMA<sup>high</sup>IL-6<sup>-</sup>) and pure iCAFs ( $\alpha$ SMA<sup>-</sup>IL-6<sup>high</sup>), warranting further investigation. These additional subtypes could represent hybrid or intermediate CAF states, although this concept has not yet been fully explored. Similarly, scRNA-seq analysis in human bladder cancer identified iCAFs expressing *IL6*, *CXC* motif chemokine ligand 12 (*CXCL12*), and *CXCL14*, which are distinct from myCAFs (24). However, the underlying biology governing the conversion between iCAFs and myCAFs and their clinical relevance are still at its early stage of investigation.

Cytotoxic chemotherapy remains the standard of care for many epithelial tumors. In the past decades, most studies have focused on optimizing chemotherapy efficacy by enhancing direct cytotoxic effects to increase programmed cell death in epithelial cancer cells. However, recent studies have revealed that cell death–associated biology plays a broader role beyond tumor cell elimination. These processes can influence residual cancer cell repopulation, trigger compensatory proliferation (25), and induce immunosuppression in the TME (26, 27), collectively shaping the overall chemotherapy response. Despite growing evidence linking CAFs and fibrosis to chemoresistance (19), the effects of chemotherapy-induced cell death on fibroblasts—the predominant stromal cell type in the TME—remain largely unexplored.

<sup>1</sup>Department of Urology, Methodist Neal Cancer Center, Houston Methodist Research Institute, Houston, TX 77030, USA. <sup>2</sup>Graduate Institute of Medical Sciences, Taipei Medical University, Taipei City, Taiwan. <sup>3</sup>Department of Pathology, Stanford University, Stanford, CA 94305, USA. <sup>4</sup>Graduate Program in Biomedical Sciences, Cedars-Sinai Medical Center, Los Angeles, CA 90048, USA. <sup>5</sup>Regenerative Medicine Institute, Cedars-Sinai Medical Center, Los Angeles, CA 90048, USA. <sup>6</sup>Biostatistics and Bioinformatics, H. Lee Moffitt Cancer Center, Tampa, FL 33612, USA.

\*Corresponding author. Email: hgao@houstonmethodist.org (H.G.); kschan@houstonmethodist.org (K.S.C.)

†Present address: Department of Urology, School of Medicine, Louisiana State University Health Sciences Center, New Orleans, LA 70112, USA.

Here, we uncovered distinct fibroblast subtypes in patients with bladder cancer and patient-derived CAFs. Clinically, patients with chemoresistant bladder cancer are enriched for a fibroblast gene signature driven by inflammatory fibroblast (iCAF) genes, such as *IL-6* and *PDGFR $\beta$* , while notably lacking *ACTA2*/ $\alpha$ SMA. Bioinformatic deconvolution further confirms a significant increase in iCAF proportions in patient tumor tissues postchemotherapy compared to matched prechemotherapy samples, implicating iCAFs in chemoresistance. Mechanistically, iCAF conversion is not influenced by the direct effect of chemotherapy on CAFs, but driven by chemotherapy-induced, Casp1-dependent tumor cell pyroptosis and its associated chemokines. Moreover, iCAF-derived collagen III (Col3) deposition promotes CD44<sup>high</sup> chemoresistant cancer stem cells (CSCs). Pharmaceutical inhibition of Casp1 activity effectively reduces iCAF conversion, fibrosis, and collagen III deposition, mitigating chemoresistance. This study reveals that canonical pyroptosis is indeed “inflammatory”; however, promoting an inflammatory fibrotic process that enhances chemoresistance.

These findings challenge the prevailing assumption that Casp1-dependent pyroptosis is universally beneficial to anticancer therapies. Chemotherapy-induced tumor cell pyroptosis creates an inflammatory fibrotic microenvironment that promotes chemoresistant CSCs. Our study highlights the clinical and biological importance of CAF subtypes in chemoresistance. This also raises caution to the current notion that pyroptotic cell death is not always beneficial to anticancer therapy, depending on the cell type it affects. Hence, this calls for thorough evaluation of pyroptosis-modulating drugs as anticancer therapies, depending on the treatment context.

## RESULTS

### Patients with chemoresistant bladder cancer exhibit an inflammatory fibroblast signature

Neoadjuvant chemotherapy (NAC) is the current standard of care for locally invasive muscle-invasive bladder cancer (MIBC), which only provided a modest improvement in survival benefit for patients (28). To explore mechanisms contributing to this limited response, we analyzed gene expression data from a cohort of patients with chemoresistant bladder cancer comparing matched pre- and postchemotherapy tissues (29). Gene set enrichment analysis (GSEA) (29) identified a fibroblast gene signature that was significantly enriched in postchemotherapy tumor tissues [normalized enrichment score (NES) = 2.11,  $P < 0.0001$ ; Fig. 1A], including a significant up-regulation of *COL3A1* (Fig. 1B). Other key fibroblast genes driving the enrichment included *IL6* and *PDGFRB*, but not the classical myCAF marker *ACTA2* (Fig. 1C). *IL6* is a cytokine and commonly used as an inflammatory marker for iCAFs in other cancer types such as pancreatic cancers (21), while *PDGFRB*<sup>+</sup> CAFs remain relatively unexplored in bladder cancer. These clinical findings suggest a subtype of fibroblasts, potentially iCAFs, in conferring chemotherapeutic resistance in human bladder cancer.

To investigate this concept, we use multiplex immunohistochemistry (mxIHC) to costain  $\alpha$ SMA (red) with *PDGFR $\beta$*  (green), Col3 (gray), and *IL-6* (magenta) in human bladder cancer patient tissue sections (Fig. 1D). This allowed us to evaluate their colocalization and identify different CAF subtypes labeled by these protein markers (Fig. 1, D to F, and fig. S1, A and B). Region 1 revealed  $\alpha$ SMA<sup>+</sup>*PDGFR $\beta$* <sup>+</sup> CAFs (Fig. 1E and fig. S1; red  $\alpha$ SMA and green *PDGFR $\beta$*  costain), and region 2 revealed  $\alpha$ SMA<sup>-</sup>*PDGFR $\beta$* <sup>+</sup> CAFs

(Fig. 1F and fig. S1; green *PDGFR $\beta$*  stain only). Notably, most CAFs in both regions 1 and 2 also express *IL-6*, a marker previously thought to exclusively identify iCAFs. The existence of these  $\alpha$ SMA<sup>+</sup>*IL-6*<sup>+</sup> bladder CAFs in region 1 has been previously reported elsewhere in a transgenic mouse model of pancreatic cancer (23). Such an observation led us to hypothesize that certain CAFs may exist in a “hybrid” state, coexpressing both myCAF ( $\alpha$ SMA) and iCAF (*IL-6*) markers.

To generalize these mxIHC observations, we analyzed scRNA-seq datasets from bladder cancers and unbiasedly subclustered CAFs into distinct subtypes (Fig. 1G). These CAF subtypes recapitulated our mxIHC observations, which include (i) myCAFs, which are *ACTA2*<sup>high</sup> and *IL6*<sup>-</sup> (Fig. 1, G to I); (ii) iCAFs, which are *ACTA2*<sup>low/-</sup> and *IL6*<sup>+</sup>, analogous to iCAFs described in Fig. 1F region 2; (iii) hybrid i/myCAFs, which are *ACTA2*<sup>+</sup> and *IL6*<sup>+</sup> (Fig. 1, G and H), analogous to CAFs described in Fig. 1E region 1 that are labeled with \*; and (iv) double-negative CAFs (DNCAFs) with *ACTA2*<sup>low/-</sup> and *IL6*<sup>low/-</sup> (Fig. 1, G and H). To better understand the biological features of these CAF subtypes, we illustrated key genes associated with their functions in a dot plot (Fig. 1I). Consistent with Fig. 1 (D to H), both myCAFs and hybrid i/myCAFs expressed *ACTA2* as well as *MYH11*. Notably, hybrid i/myCAFs also coexpress several cytokine genes typically characteristic of iCAFs, these include *CCL2*, *CCL19*, *IL6*, and *CXCL12*. DNCAFs displayed expression of *PDPN* and *PDGFRA* shared with iCAFs and *WNT5A* with myCAFs; additionally, DNCAFs seem to be more proliferative with the expression of *MKI67*. Figure S1C denotes the top 20 cluster-defining genes for distinguishing CAF clusters (Fig. 1, G to I). To further establish the clinical relevance of these CAF subtypes in bladder cancer chemoresistance, we performed digital deconvolution (30) using the top 20 CAF cluster-specific genes to bioinformatically estimate their relative proportions in a chemoresistant patient cohort. Digitally deconvoluted iCAFs and hybrid i/myCAFs, but not myCAFs or DNCAFs, were significantly increased in chemoresistant patients after treatment (Fig. 1J). This elevation of iCAFs in chemoresistant bladder cancers is similar to the recently reported iCAFs in chemoresistant pancreatic cancers (31). Together, these findings support the notion that distinct CAF subtypes exist in human bladder cancer patients and highlight the clinical relevance of iCAFs and iCAF-related genes (i.e., *IL6*) in association with chemoresistance.

*COL1A1*, *COL1A2*, and *COL3A1* are highly expressed in myCAFs, iCAFs, and DNCAFs but not hybrid i/myCAFs (fig. S1C). These collagen levels were significantly higher than that in other structural stromal cells, such as endothelial cells. This aligns with the previous reports on bladder CAFs regarding collagen type I (24) and III expressions (32). Given that pericytes also express *COL1A1* and *COL3A1* (33), we distinguished and excluded pericytes from stromal fibroblasts by their high coexpression of *MCAM* and *RGS5* (34). This pericyte exclusion strategy was supported by a pericyte gene signature (35), illustrating that it was most specific to the *MCAM*<sup>high</sup>*RGS5*<sup>high</sup> pericyte cluster (fig. S2A). Hybrid i/myCAFs intermediately expressed pericyte markers, such as melanoma cell adhesion molecule (*MCAM*) and *CSPG4*. To further characterize the expressions of these markers, we performed mxIHC for *MCAM* (CD146) and neuron-gial antigen (NG2, *CSPG4*) in bladder cancer samples (fig. S2B).

Consistent with gene signatures, *MCAM* was highly expressed in vascular structures, identifying pericytes (fig. S2B). *MCAM* can also be observed in hybrid i/myCAFs and myCAFs (fig. S2B, \* and # respectively), as well as tumor cell regions, although at lower levels

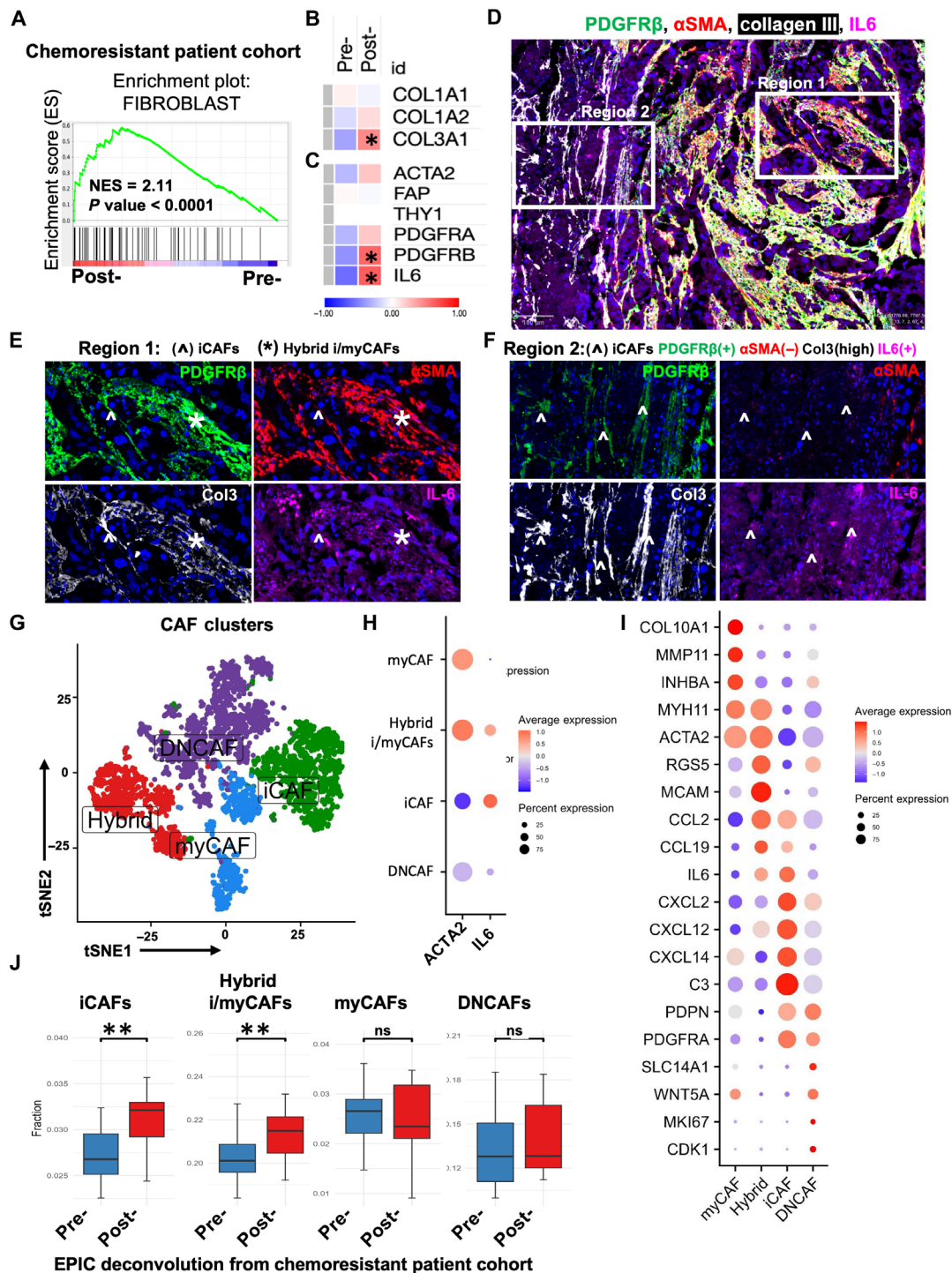


**Fig. 1. Patients with chemoresistant bladder cancer exhibit an inflammatory fibroblast signature.** (A) GSEA revealing a fibroblast gene signature enrichment in patients with chemoresistant bladder cancer (NES = 2.11,  $P < 0.0001$ ). (B and C) Heatmaps display relative expression of *COL1A1*, *COL1A2*, and *\*COL3A1* (B) and key fibroblast markers, e.g., *ACTA2*, *FAP*, *THY1*, *PDGFRA*, *\*PDGFRB*, and *\*IL6* (C) within the fibroblast signature, \* denotes statistical significance. (D) mxIHC reveals CAF heterogeneity, showing differential PDGFR $\beta$ ,  $\alpha$ SMA, Col3, and IL-6 expression in tumor tissue sections from patients with MIBC. (E) Region 1 highlights hybrid i/myCAFs (\*) coexpressing  $\alpha$ SMA (a myofibroblastic myCAF marker), PDGFR $\beta$ , and IL-6 (an inflammatory iCAF marker), with few iCAFs ( $\wedge$ ) lacking  $\alpha$ SMA but expressing PDGFR $\beta$ /IL-6. Both hybrid i/myCAFs and iCAFs colocalize Col3. (F) Region 2 shows a prevalence of iCAFs ( $\wedge$ ) with low/no expression of  $\alpha$ SMA and high expression of PDGFR $\beta$ , IL-6, and Col3. (G) t-Distributed stochastic neighbor embedding (tSNE) plot illustrating various CAF subclusters from human bladder cancer clinical cohorts, designated as myCAFs, hybrid i/myCAFs, iCAFs, and double-negative CAFs (DNCAFs). (H) Dot plot compares *ACTA2* and *IL6* expression among myCAFs, hybrid i/myCAFs, iCAFs, and DNCAFs. (I) Dot plot illustrating the normalized expression of fibroblast marker genes among CAF subclusters. Color scheme represents z score distribution from -1 (red) to 1 (blue). (J) EPIC deconvolution analysis of chemoresistant bulk RNA-seq data to assess CAF subpopulations' alterations upon NAC. ns, not significant; \*\* $P < 0.01$ .

than in pericytes. Similarly, NG2 showed intermediate expression in the intratumoral areas, colocalizing with  $\alpha$ SMA<sup>+</sup>PDGFR $\beta$ <sup>+</sup> hybrid i/myCAFs (fig. S2C), while stronger NG2 staining was observed around tumors (fig. S2C, left). This is consistent with observations from Bartoschek *et al.* (36), reporting CSPG4<sup>med</sup> CAFs after filtering out NG2<sup>+</sup> pericytes via flow cytometry. Collectively, these findings revealed that hybrid i/myCAFs express intermediate expression of pericyte markers. iCAF expansion is associated with patients with chemoresistant bladder cancer (Fig. 1J).

### Morphologically distinct myCAFs, iCAFs, and hybrid i/myCAFs coexist *ex vivo*

To investigate the role of CAFs or iCAFs in regulating chemotherapy response, we isolated human CAFs from patients with MIBC for phenotypic, molecular, and functional investigations (fig. S3A). We found that bladder CAFs uniformly express vimentin (fig. S3B) that is in line with CAFs from prostate cancer and other cancer types (37). Most *in vitro* functional studies in the past decade denote CAFs as  $\alpha$ SMA<sup>high/+</sup> myfibroblasts or myCAFs (21). Most of these fibroblasts exhibit a typical myfibroblastic cellular morphology as large stellate-shaped mesenchymal cells with positive or high  $\alpha$ SMA staining fibers in two-dimensional cultures (Fig. 2A, i). Other morphologically distinct CAF subpopulations lacking  $\alpha$ SMA staining can be characterized as spindle-shaped (Fig. 2A, ii) and a small round-shaped morphology (Fig. 2A, iii). The identity of these  $\alpha$ SMA<sup>-</sup> CAFs is unknown and warrants further investigation.

To characterize  $\alpha$ SMA<sup>-</sup> CAFs, we performed immunofluorescence (IF) costaining using markers  $\alpha$ SMA and IL-6 on CAFs cultured short-term (~16 hours). Notably, IF costaining revealed a distinct  $\alpha$ SMA<sup>-</sup> IL-6<sup>+</sup> subpopulation (Fig. 2B, red, \*) smaller than neighboring  $\alpha$ SMA<sup>+</sup> IL-6<sup>-</sup> myCAFs (Fig. 2B, green). These two CAF subtypes accounted for 37 and 28%, respectively (Fig. 2C, pie chart). We independently performed IF costaining using  $\alpha$ SMA and PDGFR $\beta$  to further characterize CAFs. PDGFR $\beta$  preferentially stained small and round-shaped CAFs without  $\alpha$ SMA expression, accounting for ~25% of CAFs (Fig. 2D, red, \*). These data suggest that smaller CAFs likely coexpress the typical iCAF marker IL-6 and PDGFR $\beta$  at the protein level.

### IL-6<sup>+</sup> CAFs compose of iCAFs and hybrid i/myCAFs

To characterize the smaller-sized CAFs described in Fig. 2 (A to E), we designed a multicolor spectral flow cytometry staining panel (table S1) to define the heterogeneity of bladder CAFs using previously reported markers (13, 38), including  $\alpha$ SMA, CD90, fibroblast activation protein (FAP), PDGFR $\alpha$ , PDGFR $\beta$ , IL-6, and major histocompatibility complex class II (16). To this end, we were able to classify monolayer cultured CAFs into 15 distinct cell clusters using the Flow Self-organizing Maps (FlowSOM) algorithm, based on their similarities in a Minimum Spanning Tree (Fig. 2, F and G). We identified two major branches of CAFs, i.e.,  $\alpha$ SMA<sup>low/-</sup> (Fig. 2F, red) and  $\alpha$ SMA<sup>high/+</sup> (Fig. 2F, green). Eight clusters characterized as  $\alpha$ SMA<sup>high/+</sup> CAFs (pops 0 to 4, 10, 11, and 13) formed the right branch, accounting for ~64% of cells, while seven  $\alpha$ SMA<sup>low/-</sup> CAF subgroups (pops 5 to 9, 12, and 14) formed the left branch, comprising ~36% (Fig. 2F and fig. S3, C and D). Three  $\alpha$ SMA<sup>high/+</sup> subpopulations (pops 0, 1, and 2; total 10%) displayed typical  $\alpha$ SMA<sup>high/+</sup> IL-6<sup>low/-</sup> pure myCAF characteristics (Fig. 2F and fig. S3, C and D). We identified and described five  $\alpha$ SMA<sup>high/+</sup> subsets (pops 3, 4, 10, 11, and 13) coexpressing IL-6 as hybrid i/myCAFs that made up

about 54% of all CAFs (Fig. 2F and fig. S3, C and D), confirming mxIHC costain in Fig. 1 (D and E) and scRNA-seq findings we reported in Fig. 1 (G to I) (blue cluster: hybrid i/myCAFs).

Next, we examined the relationship between IL-6 and PDGFR $\beta$  to determine whether they label the same CAFs at the protein level and to reveal additional quantitative information to Fig. 2 (A to E). uniform manifold approximation and projection (UMAP) clustering showed a positive correlation between IL-6<sup>+</sup> and PDGFR $\beta$ <sup>+</sup> CAF clusters, specifically pops 4, 10, 11, 13, and 14 (Fig. 2H and fig. S3, C and D). IL-6<sup>high</sup> CAFs consistently coexpressed PDGFR $\beta$  over 8 days of monolayer culturing (Fig. 2I). Long-term monolayer culturing on hard plastic surface primed CAFs into  $\alpha$ SMA<sup>high/+</sup> CAFs (fig. S3E). After 8 days, most CAFs (~85%) became  $\alpha$ SMA<sup>high/+</sup> CAF and coexpressed IL-6 as the  $\alpha$ SMA<sup>high/+</sup> IL-6<sup>+</sup> hybrid i/myCAF phenotype, while the remaining (~14.7%) were  $\alpha$ SMA<sup>high/+</sup> IL-6<sup>-</sup> pure myCAFs (fig. S3F). Thus, PDGFR $\beta$  expression is closely associated with IL-6 expression at the protein level in bladder CAFs, posing PDGFR $\beta$  as a surrogate cell surface marker for IL-6<sup>+</sup> CAFs *in vitro*. Bladder CAFs in monolayered culture are predominantly hybrid i/myCAFs rather than pure myCAFs as previously thought, representing another insight revealed by multicolor flow cytometry.

### Chemotherapy-induced tumor cell pyroptosis converts $\alpha$ SMA<sup>high/+</sup> CAFs into iCAFs

To evaluate how CAFs respond to chemotherapy, we first compared the responses of CAFs and T24 bladder cancer cells to a dose escalation of gemcitabine treatment. *In vitro* gemcitabine treatment revealed that CAFs were remarkably resistant to gemcitabine [median inhibitory concentration (IC<sub>50</sub>) > 900  $\mu$ M] (Fig. 2J, red squares), consistent with previous reports in breast cancers (22). In contrast, T24 bladder cancer cells were much more sensitive (IC<sub>50</sub> = ~0.5  $\mu$ M) (Fig. 2J, blue dots). We also observed a dose-dependent decrease in *ACTA2* (Fig. 2K, blue line) and corresponding increase in *IL6* expression (Fig. 2K, red line). Since *ACTA2* and *IL6* are surrogate markers for myCAFs and iCAFs, respectively, these initial findings support clinical findings from Fig. 1 (A to C) that iCAFs might be functionally relevant to chemoresistance, prompting us to further evaluate CAF subtype changes in response to chemotherapy.

To determine whether chemotherapy-treated cancer cells affect CAF subtypes, we exposed bladder CAFs to conditioned medium (CM) collected from T24 bladder cancer cells treated with or without gemcitabine (0.5  $\mu$ M, 48 hours) (schematic Fig. 3A). CM from gemcitabine-treated cancer cells (Gem) significantly increased  $\alpha$ SMA<sup>low/-</sup> CAFs from ~2 to 28.5% (Fig. 3, B to D; CM-Gem versus CM-Veh). The CM from vehicle T24 (Veh) maintained CAF subpopulations similar to basic medium [2% fetal bovine serum (FBS) Dulbecco's modified Eagle's medium (DMEM)] (Fig. 3, B and D).  $\alpha$ SMA<sup>low/-</sup> CAFs treated with CM-Gem primarily composed of PDGFR $\beta$ <sup>+</sup> CAFs (Fig. 3B, green box) which coexpressed high levels of IL-6 and, therefore, designated as iCAFs ( $\alpha$ SMA<sup>low/-</sup>PDGFR $\beta$ <sup>+</sup>IL-6<sup>+</sup>) hereafter (Fig. 3, D and E). These results suggest that certain chemokines or cytokines released from gemcitabine-treated bladder cancer cells are likely playing a role in converting  $\alpha$ SMA<sup>high/+</sup> CAFs into iCAFs.

Others and our previous studies have revealed that chemotherapy effectively induces programmed cell death in differentiated bladder cancer cells (25). We previously discovered that dying cancer cells release mitogens and chemokines extracellularly, affecting neighboring cells in a paracrine manner (25–27). Although CAFs

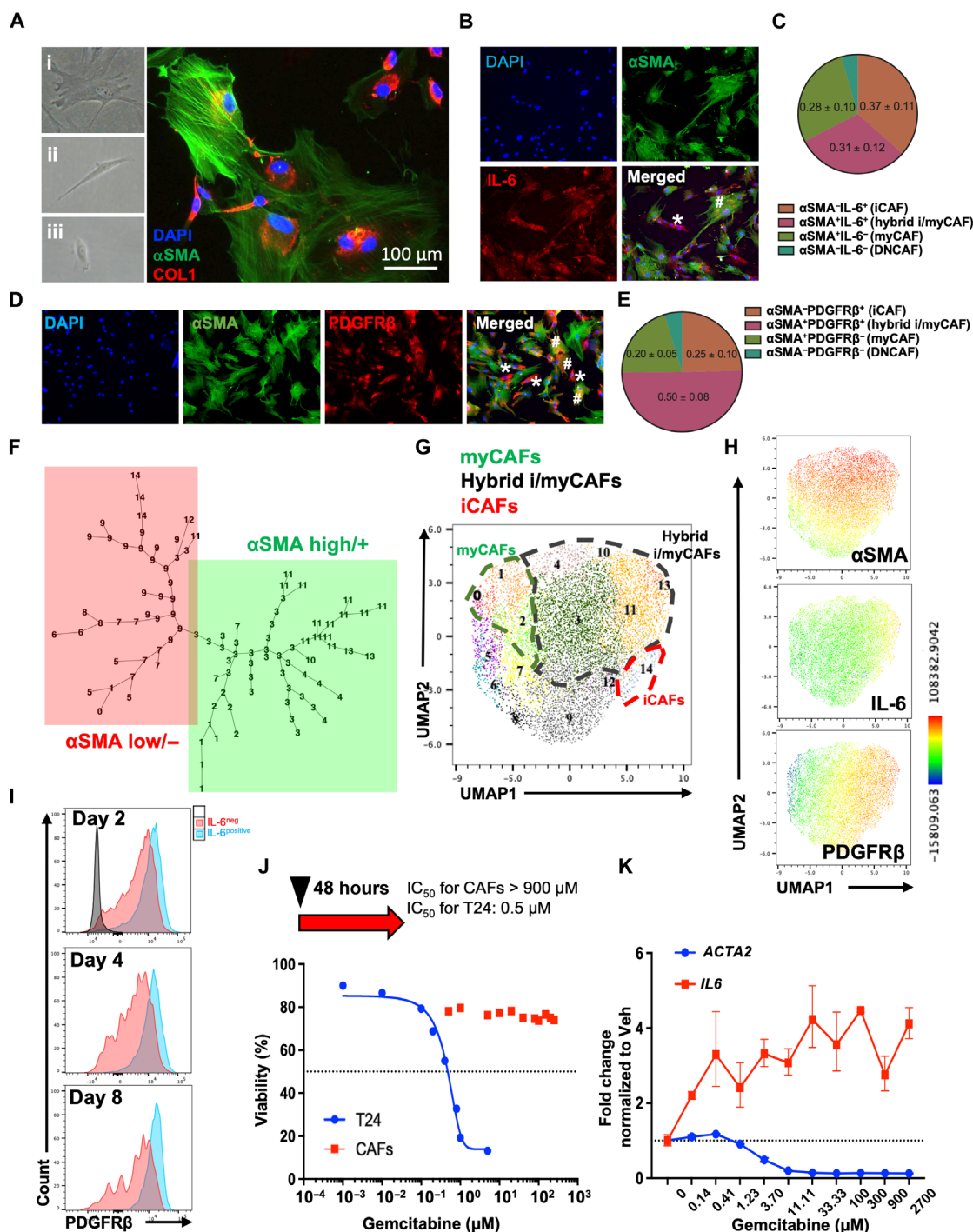


**Fig. 2. Phenotypically distinct myCAFs, iCAFs, and hybrid i/myCAFs coexist ex vivo.** (A) Bright-field images showing morphologically distinct fibroblasts within human bladder cancer patient-derived CAFs, these include (i) large stellate-shaped CAFs with stress fibers, (ii) spindle-shaped CAFs, and (iii) small, round-shaped CAFs. IF costain illustrating the myofibroblastic marker  $\alpha$ SMA (green) and collagen I expression across CAF subtypes. (B) IF costain showing the colocalization of  $\alpha$ SMA—a myofibroblastic marker (green), and IL-6—an inflammatory marker (red) in CAFs. (C) A pie chart qualifies CAF subtypes based on  $\alpha$ SMA and IL-6 costaining. (D) IF costained  $\alpha$ SMA (green) and PDGFR $\beta$  (red) in CAFs. (E) A pie chart quantifies CAF subtypes marked by  $\alpha$ SMA and PDGFR $\beta$ . (F) Cytek multiplex flow cytometry analysis of CAFs using a panel of fibroblast markers, visualized using Minimum Spanning Tree into 14 CAF subpopulations that are assigned into multidimensional nodes based on their similarities. Briefly, these CAFs are subdivided into two major sub-branches:  $\alpha$ SMA<sup>high/+</sup> (green) and  $\alpha$ SMA<sup>low/-</sup> (red). (G) UMAP plot generated using FlowSOM to visualize the heterogeneity of CAFs, including myCAFs, iCAFs, and hybrid i/myCAFs. (H) UMAP illustrating  $\alpha$ SMA, IL-6, and PDGFR $\beta$  expression in CAFs. (I) Flow cytometry analysis evaluating the expression dynamics of PDGFR $\beta$  in IL-6<sup>+</sup> (blue) and IL-6<sup>-</sup> (red) CAFs over an 8-day monolayer culture, confirming that IL-6<sup>+</sup> CAFs are also PDGFR $\beta$ <sup>+</sup>. (J) Treatment of T24 bladder cancer cells (blue line) and CAFs (red line) with dose escalation of gemcitabine chemotherapy for 48 hours in vitro. (K) Quantitative polymerase chain reaction (qPCR) analysis quantifying *ACTA2* (gene name for  $\alpha$ SMA, blue line) and *IL6* (red line) expression in CAFs treated with increasing dosage of gemcitabine.

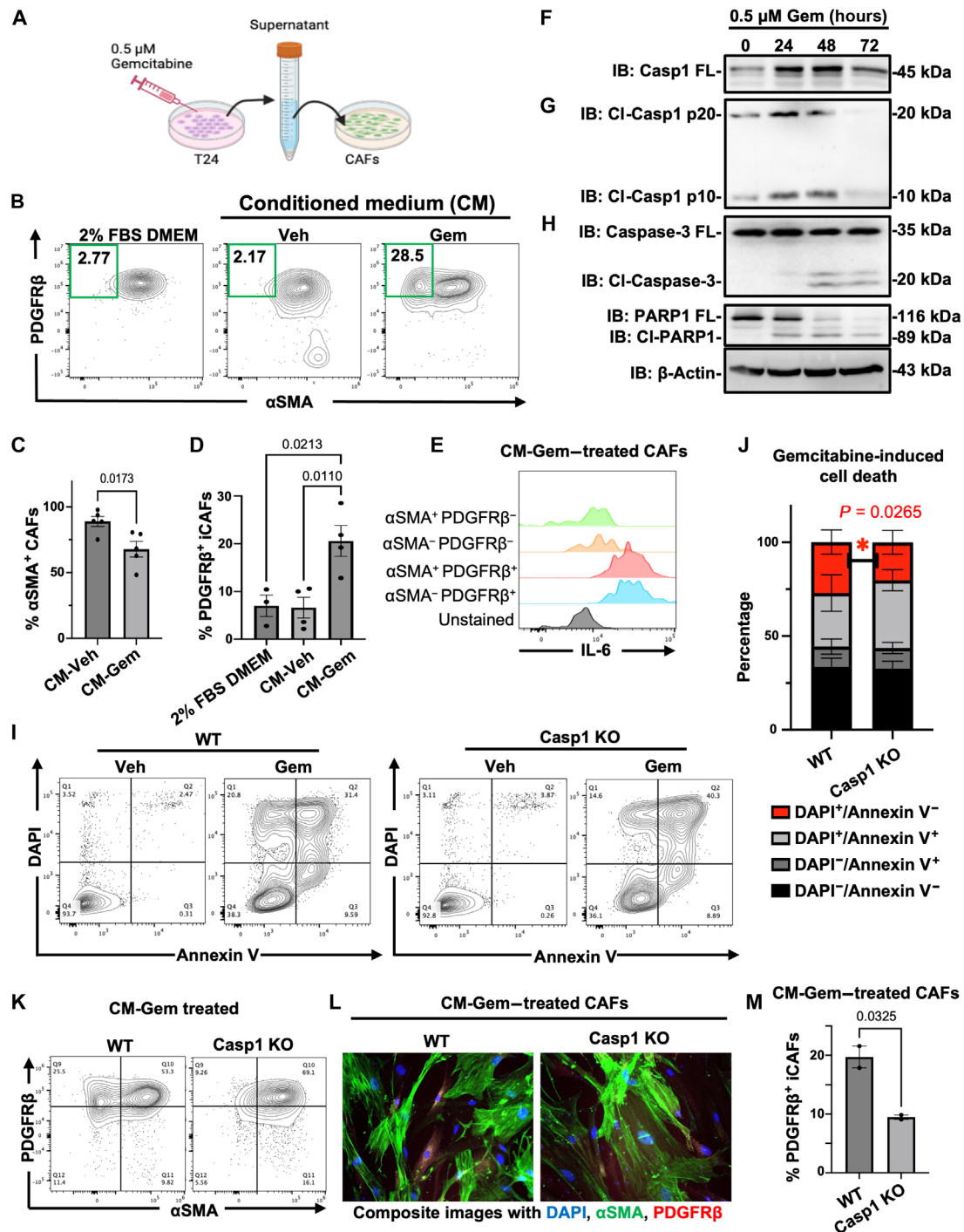


**Fig. 3. Chemotherapy-induced tumor pyroptosis converts αSMA<sup>high/+</sup> CAFs into iCAFs.** (A) Schematic of CM from chemotherapy-treated cancer cells for subsequent treatment on CAFs in vitro. (B) Flow cytometry evaluating CM effects on αSMA<sup>high/+</sup> CAFs and αSMA<sup>low/-</sup> PDGFRβ<sup>+</sup> iCAF conversion, in response to (i) base medium (2% FBS DMEM), (ii) CM from untreated T24 (CM-Veh), and (iii) CM from gemcitabine-treated T24 (CM-Gem). (C and D) Bar graphs quantifying αSMA<sup>high/+</sup> CAFs (C) and αSMA<sup>low/-</sup> PDGFRβ<sup>+</sup> iCAFs (D) upon treatment with CM-Veh and CM-Gem. (E) Flow cytometry histogram illustrating higher IL-6 expression in αSMA<sup>+</sup> PDGFRβ<sup>+</sup> iCAFs (blue) and αSMA<sup>+</sup> PDGFRβ<sup>+</sup> hybrid i/my CAFs (red) than other CAFs (green and yellow). (F to H) Western blot analysis of Casp1-dependent pyroptosis and apoptosis in gemcitabine-treated T24 cells by immunoblotting (IB): (F) Casp1 full-length (FL) protein, (G) Casp1 p20 and p10 cleavage (CI) products indicating enzymatic activity, and (H) Caspase-3 (Casp3) FL, CI-Casp3, and DNA repair protein poly(ADP-ribose) polymerase 1 (PARP1) FL and CI PARP1 (CI-PARP1), as apoptosis markers. (I) Flow cytometry of DAPI and annexin V costaining in WT and Casp1 knockout (Casp1 KO) T24 cells upon gemcitabine treatment. (J) Bar graph quantifying fractions in (I), showing reduced lytic cell death (DAPI<sup>+</sup>/annexin V<sup>-</sup>; red) in Casp1 KO cells (\*P = 0.0265). (K) Flow cytometry analyzing CM from gemcitabine-treated WT or Casp1 knockout (Casp1 KO) T24 cells in the conversion between αSMA<sup>high/+</sup> CAFs and αSMA<sup>low/-</sup> PDGFRβ<sup>+</sup> iCAFs. (L) Corresponding IF costaining illustrating PDGFRβ (red) and αSMA (green) in CAFs exposed to CM-Gem from T24 WT and Casp1 KO cells. (M) Bar graph quantifying PDGFRβ<sup>+</sup> iCAFs, showing significant reduction after exposure to CM-Gem from Casp1 KO versus WT cells.

are a predominant stromal cell type localized adjacent to tumor cell clusters in patient tissues, the cross-talk between chemotherapy-induced cancer cell death and CAFs remains to be elucidated. Here, we found that gemcitabine induced various types of programmed cell death, including the classical caspase-3 (Casp3)-dependent apoptosis and a Casp1-dependent pyroptosis (Fig. 3, F to H). Chemotherapy-induced canonical pyroptosis in bladder cancer cells is illustrated by cleaved (Cl)-Casp1 (p20 and p10) (Fig. 3F). Cl-Casp1, increased at 24 and 48 hours (Fig. 3F), which preceded apoptotic Cl-Casp3 and poly(ADP-ribose) polymerase 1 (PARP-1; a DNA repair protein and substrate of Casp3) cleavage, peaking at 48 hours postchemotherapy (Fig. 3, G and H).

To evaluate whether Casp1-driven tumor pyroptosis affects CAF subtypes, we used CRISPR-Cas9 technology to genetically knockout Casp1 (Casp1 KO) in T24 cancer cells. In response to gemcitabine treatment, Casp1 KO cancer cells conserved Cl-Casp3 (i.e., apoptosis) at 48 hours (fig. S4A). Furthermore, genetic depletion of Casp1 significantly diminished lytic cell death and pyroptosis induced by the canonical pyroptosis inducers—lipopolysaccharide and nigericin [fig. S4B; 4',6-diamidino-2-phenylindole (DAPI)<sup>+</sup> annexin V<sup>-</sup> subset], validating that Casp1 is important for driving pyroptosis in bladder cancer cells. In response to gemcitabine, Casp1 KO T24 cells significantly reduced lytic cell death and pyroptosis (DAPI<sup>+</sup> annexin V<sup>-</sup> subset) compared with wild-type (WT) T24 cells (Fig. 3, I and J, red;  $P = 0.03$ ), supporting that gemcitabine-induced pyroptosis is also Casp1 dependent. We then exposed CAFs to CM from gemcitabine-treated Casp1 KO versus WT T24 cells. We observed a significant reduction in PDGFR $\beta$ <sup>+</sup> iCAF, illustrated by flow cytometry (Fig. 3K; 25.5 to 9.26%) and IF staining (Fig. 3, L and M; 20 to 10%), indicating that gemcitabine-mediated PDGFR $\beta$ <sup>+</sup> iCAF conversion depends on epithelial Casp1 function. In summary, gemcitabine-induced Casp1-dependent pyroptosis contributes to the conversion of  $\alpha$ SMA<sup>high/+</sup> CAFs into an  $\alpha$ SMA<sup>low/-</sup>PDGFR $\beta$ <sup>+</sup> iCAF subset.

### Tumor cell pyroptosis skews CAFs toward iCAFs in a CCR6-dependent mechanism

To identify cytokines or chemokines released by Casp1-mediated pyroptotic cancer cells that drive PDGFR $\beta$ <sup>+</sup> iCAF conversion, we used a cytokine/chemokine array to compare the CM collected from gemcitabine-treatment WT and Casp1 KO T24 cells (Fig. 4A). Several cytokine/chemokines, including CXCL5, CXCL10, and CCL20, were significantly reduced in CM from gemcitabine-treated Casp1 KO cells (Fig. 4, A and B). Consistently, enzyme-linked immunosorbent assay (ELISA) assay confirmed the reduction in these proteins (Fig. 4C). Thus, this prompted us to evaluate their functional role in regulating PDGFR $\beta$ <sup>+</sup> iCAF conversion. We treated CAFs using CM as previously described, in combination with neutralizing antibodies (Abs) and a pharmaceutical inhibitor against the corresponding cytokine receptors, including anti-CXCR2, anti-CXCL10, anti-CCL20 Abs, and CCR6 inhibitor (CCR6i). To this end, we found that inhibition of CCR6 significantly suppressed iCAF conversion (Fig. 4, D and E), while the effects of anti-CXCR2, anti-CXCL10, or anti-CCL20 were not observed.

### Gemcitabine-induced iCAFs reactively express Col3

To recapitulate the effects of tumor-to-CAF cross-talk in affecting CAF heterogeneity, we cocultured T24 cancer cells with CAFs and performed flow cytometry to examine IL-6,  $\alpha$ SMA, and PDGFR $\beta$

expression in CAFs after coculture (Fig. 5A). After 4 days of coculture, ~35% of CAFs shifted to an  $\alpha$ SMA<sup>low/-</sup> population, and 11.7% of CAFs exhibited iCAF phenotype as  $\alpha$ SMA<sup>low/-</sup>IL-6<sup>+</sup> subpopulation (Fig. 5A, red box and curve); whereas 38.6% CAFs preserved  $\alpha$ SMA and IL-6 expression as hybrid i/myCAFs (Fig. 5A, blue box and curve). PDGFR $\beta$  is shown to be a surrogate cell surface marker for IL-6<sup>+</sup> CAFs, since PDGFR $\beta$  expression is high in  $\alpha$ SMA<sup>low/-</sup>IL-6<sup>+</sup> iCAFs (Fig. 5A, red curve), intermediate in  $\alpha$ SMA<sup>high</sup>IL-6<sup>high</sup> CAFs (blue curve), low in  $\alpha$ SMA<sup>high</sup>IL-6<sup>low</sup> myCAFs (yellow curve), and absent in  $\alpha$ SMA<sup>low/-</sup>IL-6<sup>-</sup> CAFs (green box and curve). IF costaining confirmed that PDGFR $\beta$  was highly expressed in  $\alpha$ SMA<sup>low/-</sup> iCAFs and undetectable in  $\alpha$ SMA<sup>high</sup> myCAFs (Fig. 5B).

We next evaluate the effects of gemcitabine in this cancer-CAF coculture system as an ex vivo model. Cocultured cells were exposed to gemcitabine for 48 hours followed by a resting phase of 96 hours by replacing the culture with fresh medium (fig. S5A), such treatment scheme is designed to recapitulate the clinical cyclical chemotherapy regimen. Eight days of cancer-CAF coculture further reduced  $\alpha$ SMA<sup>+</sup> CAF subtype to 20%, compared with 90%  $\alpha$ SMA<sup>+</sup> CAFs when CAFs are maintained in monolayer culture [fig. S5 (B and C) versus fig. S3 (D and E)], and the cellular morphology of CAFs in coculture was converted into smaller-sized  $\alpha$ SMA<sup>low/-</sup> CAFs (fig. S5D, top: Veh coculture). Despite reduced  $\alpha$ SMA expression, CAFs retained PDGFR $\beta$  expression in cancer-CAF coculture, and PDGFR $\beta$ <sup>+</sup> iCAFs accounted for 28.3% of total CAFs (fig. S5, B and C). IF costaining revealed that PDGFR $\beta$ <sup>+</sup> iCAFs were sparsely distributed among confluent cancer cells (fig. S5D, top: Veh coculture, \* denoted for iCAFs, and # denoted for hybrid i/myCAFs).

In response to one gemcitabine treatment cycle, the proportion of iCAFs in this coculture system accounted for 35.1% (fig. S5B, red box), reproducing the effects of CM-Gem from Fig. 3B. iCAFs are scattered with low  $\alpha$ SMA expression (fig. S5D, middle, ^ labeled) which locate adjacent to hybrid CAF clusters coexpressing  $\alpha$ SMA and PDGFR $\beta$  (fig. S5C, middle, labeled by \*). After 1 cycle of gemcitabine treatment, the residual surviving bladder cancer cells ( $\Delta$ ) are distributed closely adjacent to CAFs (fig. S5C, middle). Our findings here implicate that the direct cancer cell-CAF contact restricted the expansion of CAFs during treatment-naïve scenario. During chemotherapy, induction of cancer cell death and pyroptosis removed this physical contact inhibition, thus allowing CAF expansion which serves as a niche for surviving cancer cells.

Next, we investigate the mechanism by which iCAFs influence residual surviving cancer cells and their repopulation. Connecting to clinical findings from Fig. 1 (A to C and J) revealing that patients with chemoresistant bladder cancer exhibit a correlative increase of iCAF markers (*IL6* and *PDGFRB*) and *COL3A1*, we hypothesized that ex vivo expanded PDGFR $\beta$ <sup>+</sup> iCAFs in response to chemotherapy might produce Col3 to exert relevant biologic functions. To prospectively isolate iCAFs and other CAF subtypes for evaluating their corresponding collagen gene expressions, we use FAP as a surrogate cell surface marker for  $\alpha$ SMA (since  $\alpha$ SMA is an intracellular protein found to positively associate with FAP expression) (Fig. 5C) (22). PDGFR $\beta$ <sup>+</sup>FAP<sup>-</sup> CAFs correspond to iCAFs, expressing IL-6 with low  $\alpha$ SMA expression (Fig. 5C, blue color). In addition, PDGFR $\beta$ <sup>+</sup>FAP<sup>+</sup> CAFs correspond to hybrid i/myCAFs, coexpressing IL-6 and  $\alpha$ SMA (Fig. 5C, red color).

By integrating fluorescence-activated cell sorting (FACS) to isolate distinct CAF subtypes, followed by flow cytometry and quantitative

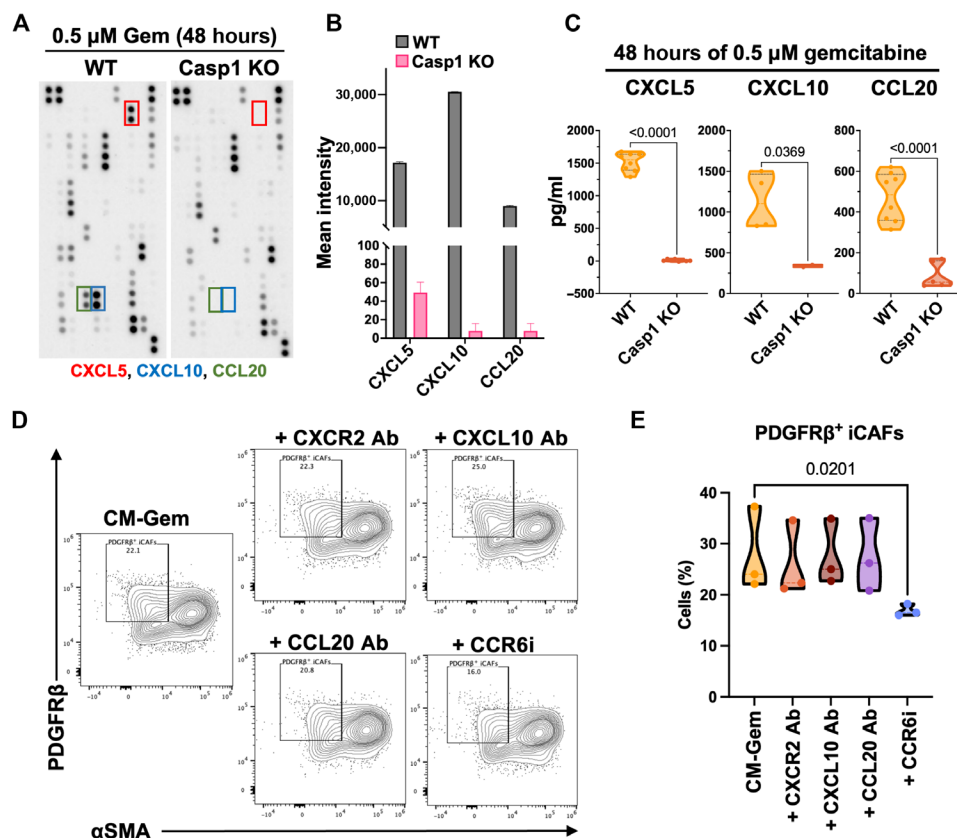


**Fig. 4. Tumor cell pyroptosis skews CAFs toward i CAFs in a CCR6-dependent mechanism.** (A) Representative image illustrating a cytokine protein array (i.e., Proteome Profiler Human XL Cytokine Array Kit, R&D Systems) probed with the supernatant collected from WT and Casp1 KO T24 cancer cells after 48 hours of gemcitabine treatment. Red, blue, and green boxes highlighting the individual cytokines or chemokines with the most differential expression (i.e., reduction) in Casp1 KO versus WT Gem-treated supernatant. (B) Bar graph quantifying the intensity of three cytokines differentially released in WT and Casp1 KO supernatant, i.e., CXCL5, CXCL10, and CCL20. (C) ELISA quantification of CXCL5, CXCL10, and CCL20 protein concentration in the supernatants collected from gemcitabine-treated WT and Casp1 KO T24 bladder cancer cells. (D) Flow cytometry assessing the percentage of  $\alpha\text{SMA}^{\text{high}/+}$  CAFs and  $\alpha\text{SMA}^- \text{PDGFR}\beta^+$  i CAFs treated with CM from Gem-treated T24 cells with anti-CXCR2 neutralizing Ab, (anti-CXCR2 Ab, blocking receptor downstream to CXCL5), anti-CXCL10 neutralizing Ab, anti-CCL20 neutralizing ab, and CCR6i (blocking receptor downstream to CCL20). (E) Violin dot plot quantifying the relative changes in the percentage of  $\alpha\text{SMA}^- \text{PDGFR}\beta^+$  i CAFs upon CM-Gem  $\pm$  chemokine or chemokine receptor neutralizing Ab treatments.

polymerase chain reaction (qPCR) analyses, these approaches allow us to evaluate the relative protein and gene expression of *IL6*, *COL3A1*, and *COL1A1* in corresponding CAF subtypes, respectively (Fig. 5, C and D, and fig. S6, A to C). In response to chemotherapy treatment regimen outline in fig. S5A, we found that the elevation of *IL6* expression was contributed by  $\text{PDGFR}\beta^+ \text{FAP}^-$  i CAFs and  $\text{PDGFR}\beta^+ \text{FAP}^+$  hybrid i/my CAFs (Fig. 5D, black versus white bars), consistent with previous findings in Fig. 2I showing a high *IL-6* expression by  $\text{PDGFR}\beta^+$  CAFs. These two sorted  $\text{PDGFR}\beta^+$  CAF subsets exhibited an increased *COL3A1* expression upon chemotherapy treatment, with the highest expression in  $\text{PDGFR}\beta^+ \text{FAP}^-$  i CAFs (Fig. 5D, black versus white bars). Conversely, *COL1A1* and *COL1A2* up-regulation was not limited to  $\text{PDGFR}\beta^+$  CAFs but other CAFs such as  $\text{PDGFR}\beta^- \text{FAP}^+$  CAFs (fig. S6C, black versus white bars).

These functional studies are consistent with the clinical observations in Fig. 1 (A to C and J), supporting that  $\text{PDGFR}\beta^+ \text{IL-6}^+$  i CAFs up-regulate *Col3* in response to chemotherapy treatment. These findings also challenge the previous notion that  $\alpha\text{SMA}^{\text{high}/+}$  CAFs are

the major contributor to collagen or extracellular matrix deposition (39), revealing that i CAFs can reactively express collagens upon chemotherapy-induced stress and/or cell death.

To further consolidate the in vivo contribution of i CAFs in *Col3* deposition, we evaluated *Col3* costaining with  $\alpha\text{SMA}^{\text{low}/-} \text{PDGFR}\beta^+$  and  $\alpha\text{SMA}^{\text{high}/+} \text{PDGFR}\beta^+$  CAFs, as well as cancer cells ( $\alpha\text{SMA}^{\text{low}/-} \text{PDGFR}\beta^-$ ) in bladder cancer xenografts. First, we showed that both  $\text{PDGFR}\beta^+$  and  $\alpha\text{SMA}^{\text{high}/+}$  CAF regions corresponded to trichrome staining—a conventional blue stain that marks most collagen fibers—within the stromal area (fig. S6C, serial tissue sections), with  $\alpha\text{SMA}^- \text{PDGFR}\beta^-$  regions outlining cancer cells intercalated by CAFs and collagen fibers in bladder cancer xenografts. On the other hand, *Col3* staining seems to be more restrictive than trichrome collagen stain (Fig. 5, E and F); we use QuPath image analysis (40) to quantitatively summarize the stroma dynamics in bladder cancer xenografts that are treated with 2 cycles of vehicle (Veh) or gemcitabine-cisplatin (GC) chemotherapy (Fig. 5, E and F). In Veh-treated xenografts, cancer cells constitute most of the tumor mass, intercalated within stromal areas with less  $\text{Col3}^+$  staining

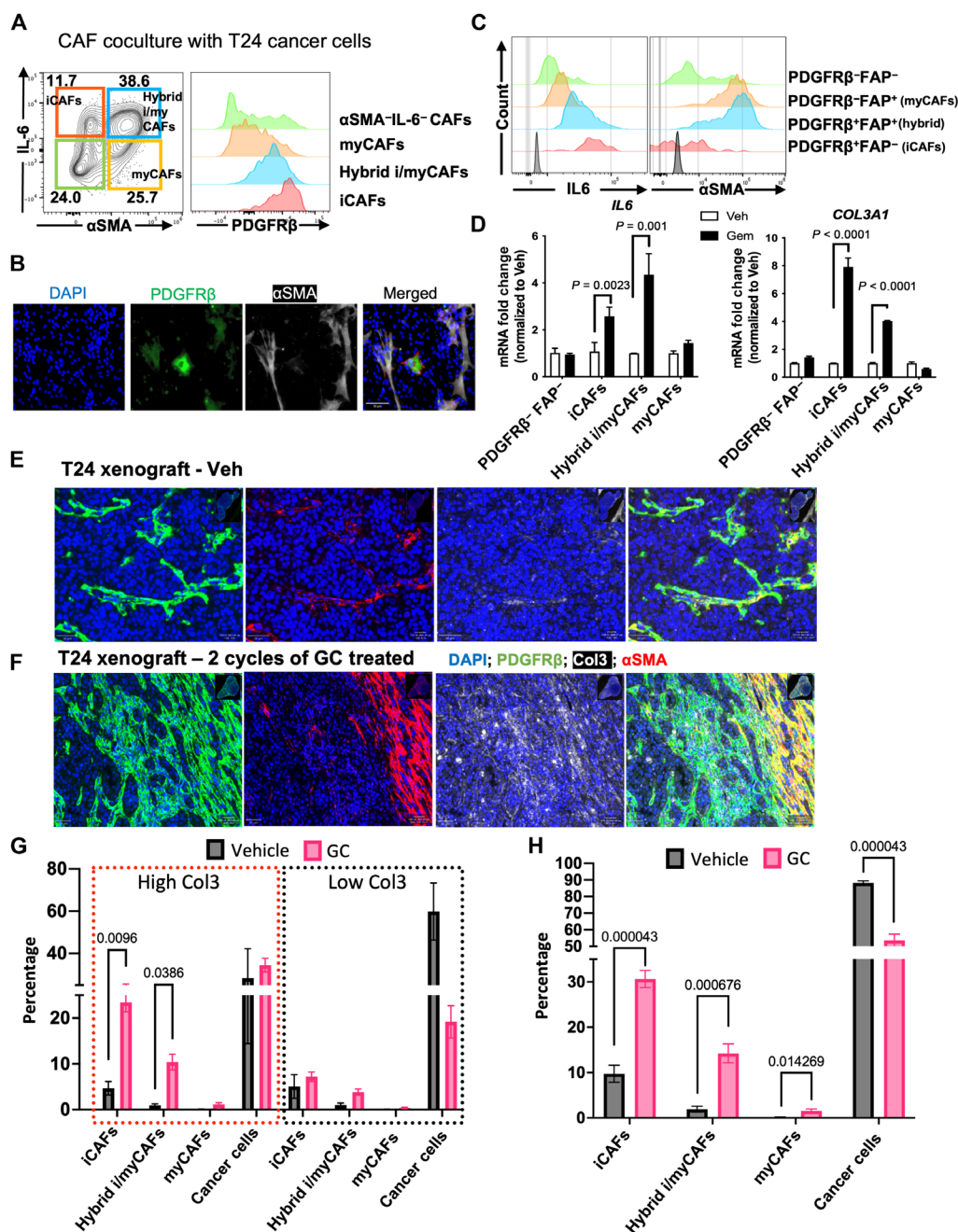


**Fig. 5. Gemcitabine-induced emergence of PDGFR $\beta$ <sup>+</sup> iCAFs reactively express Col3.** (A) Multicolor flow cytometry analyzing CAF subtypes denoted by the relative coexpression of IL-6 and  $\alpha$ SMA (left), as well as PDGFR $\beta$  (right) in CAFs cocultured with T24 cancer cells. Flow cytometry confirms the existence of (i)  $\alpha$ SMA<sup>low</sup>-IL-6<sup>+</sup> iCAFs (red box), (ii)  $\alpha$ SMA<sup>+</sup>IL-6<sup>-</sup> hybrid i/my CAFs (blue box), (iii) pure  $\alpha$ SMA<sup>+</sup>IL-6<sup>-</sup> myCAFs (yellow box), and (iv)  $\alpha$ SMA<sup>low</sup>-IL-6<sup>-</sup> CAFs (green box). Right illustrates that PDGFR $\beta$  protein expression is highly expressed in IL-6<sup>-</sup> CAFs (i.e., iCAFs and hybrid i/myCAFs) when compared with other CAF subtypes. (B) Corresponding IF costaining highlighting the smaller-shaped  $\alpha$ SMA<sup>low</sup>-PDGFR $\beta$ <sup>+</sup> iCAFs (green) and stretched stellate-shaped  $\alpha$ SMA<sup>+</sup> CAFs in coculture with T24 bladder cancer cells. (C) Flow cytometry evaluating the relative IL-6 and  $\alpha$ SMA protein expression in PDGFR $\beta$ -FAP<sup>-</sup> CAFs, PDGFR $\beta$ -FAP<sup>+</sup> myCAFs, PDGFR $\beta$ <sup>+</sup>FAP<sup>+</sup> hybrid i/myCAFs, and PDGFR $\beta$ <sup>+</sup>FAP<sup>-</sup> iCAFs, illustrating that FAP is positively associated with  $\alpha$ SMA expression, thus enabling fluorescence-activated cell sorting (FACS) in (D). (D) qPCR analysis comparing the relative *IL6* and *COL3A1* mRNA expression in FACS-purified CAF subsets upon gemcitabine treatment. In particular, PDGFR $\beta$ <sup>+</sup>FAP<sup>-</sup> iCAFs and PDGFR $\beta$ <sup>+</sup>FAP<sup>+</sup> hybrid i/myCAFs reactively up-regulate *IL6* and *COL3A1* mRNA expression upon chemotherapy treatment. (E and F) mxIHC costaining displaying the relative distribution of Col3 associated with PDGFR $\beta$ <sup>+</sup> iCAFs and  $\alpha$ SMA<sup>+</sup> CAFs in vehicle-treated xenografts (Veh, E) and two cycles of gemcitabine-cisplatin (GC) chemotherapy (F). (G) Bar graph illustrates an expansion of stromal fibroblasts after chemotherapy, which composes of  $\alpha$ SMA<sup>low</sup>-PDGFR $\beta$ <sup>+</sup> iCAFs and  $\alpha$ SMA<sup>+</sup>PDGFR $\beta$ <sup>+</sup> hybrid i/myCAFs (yellow) predominately associating with Col3 deposition. (H) Bar graphs quantifying the changes in CAF subclusters within bladder cancer xenografts after 2 cycles of GC chemotherapy treatment compared with Veh-treated control. The increase in  $\alpha$ SMA<sup>low</sup>-PDGFR $\beta$ <sup>+</sup> iCAFs upon chemotherapy treatment is most notable.

(Fig. 5, E and G). Similar to in vitro coculture that are treated with Veh as a control,  $\alpha\text{SMA}^{\text{low/-}}\text{PDGFR}\beta^+$  iCAFs represent the main CAFs in xenograft stroma colocalizing with the  $\text{Col3}^+$  area, with less  $\alpha\text{SMA}^{\text{high/+}}\text{PDGFR}\beta^+$  hybrid i/myCAFs or  $\alpha\text{SMA}^{\text{high/+}}\text{PDGFR}\beta^-$  myCAFs associating with the  $\text{Col3}^+$  area in vivo (Fig. 5, E and G).

In GC chemotherapy-treated T24 xenografts, the stromal regions were significantly expanded, evident by broader regions of trichrome staining (fig. S6D) and significantly higher density of  $\text{Col3}$ ,  $\text{PDGFR}\beta$ , and  $\alpha\text{SMA}$  staining (Fig. 5F; white, green, and red, respectively). The stromal regions marked by  $\alpha\text{SMA}^{\text{low/-}}\text{PDGFR}\beta^+$  iCAFs (green) and  $\alpha\text{SMA}^{\text{high/+}}\text{PDGFR}\beta^+$  hybrid i/myCAFs (yellow) both expanded significantly upon chemotherapy (Fig. 5, E to G). On the other hand, fiber-like  $\text{Col3}^+$  staining primarily aligned with  $\alpha\text{SMA}^{\text{low/-}}\text{PDGFR}\beta^+$  iCAF regions as well as  $\alpha\text{SMA}^{\text{high/+}}\text{PDGFR}\beta^+$  hybrid i/myCAFs but are relatively scarce in  $\alpha\text{SMA}^+$  myCAF regions upon chemotherapy (Fig. 5, F and G). Together, these findings support the notion that  $\text{PDGFR}\beta^+$  iCAFs associate with  $\text{Col3}$  deposition in response to chemotherapy.

### Pharmaceutical inhibition of Caspase 1 improves chemotherapy response

To further validate the enrichment of iCAFs in chemoresistant bladder cancer, we conducted mxIHC to detect  $\text{PDGFR}\beta$ ,  $\alpha\text{SMA}$ ,  $\text{Col3}$ ,  $\text{CD44}$ , and pan-keratin in matched pre- and postneoadjuvant bladder cancer samples. Consistent with deconvolution analysis of bulk RNA-seq (Fig. 1, A to C and J),  $\alpha\text{SMA}^{\text{low/-}}\text{PDGFR}\beta^+$  iCAFs expanded in rigorously resistant bladder cancer samples (Fig. 6, A and B), confirming findings from in vitro primary CAF studies (Fig. 3) and xenografts (Fig. 5). In addition,  $\text{Col3}$  and  $\text{CD44}$  were up-regulated in postneoadjuvant samples (Fig. 6, A and B), while pan-keratin staining remained unaffected by chemotherapy (fig. S7A).

The bioinformatic deconvolution analysis of a second independent chemoresistant bladder cancer cohort displayed the similar enhancement of iCAF and hybrid i/myCAF clusters (Fig. 6C versus Fig. 1J), with no impact on myCAFs or DNCAFs. Furthermore, patients with estimated higher proportions of iCAFs and hybrid i/myCAFs exhibited worse clinical outcomes (Fig. 6D), while patients with high components of hybrid i/myCAFs and DNCAFs were not associated with the overall survival (fig. S7, B and C). Thus, chemoresistant bladder cancer is characterized by an iCAF-predominant microenvironment, which is associated with poorer survival outcomes.

Since iCAFs colocalized with a  $\text{Col3}$  high region, we investigated the relationship of  $\text{Col3}$  with CSCs, and we found that  $\text{Col3}$  gene (i.e., *COL3A1*) expression positively correlated with  $\text{CD44}$  ( $P = 0.0012$ )—an established marker for chemoresistant CSCs (Fig. 6E) (41)—in the cohorts of patients with chemoresistant bladder cancer [shown in Fig. 6 (C and D)]. Further mxIHC imaging of bladder cancer xenografts confirmed that stromal regions with fibrillar  $\text{Col3}$ -rich staining (Fig. 6F, white color) colocalized with clusters of  $\text{CD44}^{\text{high}}$  epithelial cancer cells (Fig. 6F, yellow color, region 1), where  $\text{CD44}^{\text{low}}$  cancer cells localized farther away from these regions (Fig. 6F, region 2). These findings were quantified in Fig. 6G. Since  $\text{CD44}^{\text{high}}$  cancer cells are extensively established as CSCs with enriched tumor-initiating (42) and chemoresistant properties (43), we further explored whether functional interaction with  $\text{Col3}$  can promote  $\text{CD44}^{\text{high}}$  CSCs. Along with  $\text{CD44}$ ,  $\text{CD49f}$  (*ITGA6*) is also another common marker used for identification of CSCs (44). To

this end, we found that in vitro cotreatment of gemcitabine with  $\text{Col3}$  (25  $\mu\text{g}/\text{ml}$ ) significantly increased  $\text{CD44}^{\text{high}}\text{CD49f}^{\text{high}}$  phenotypic CSC subpopulation (Fig. 6, H and I). In contrast, treatment with  $\text{Col1}$  was incapable of increasing this population (Fig. 6, H and I), highlighting a  $\text{Col3}$ -dependent phenotype in fueling phenotypic CSCs.

We next evaluated whether pharmaceutical inhibition of Casp1-mediated pyroptosis might affect chemotherapy response through a  $\text{Col3}$  axis to expand  $\text{CD44}^+$  CSCs in vivo by using a Casp1-selective inhibitor, VX-765. Combined treatment of VX-765 with GC chemotherapy led to a significant reduction in bladder xenograft tumor volume (Fig. 6J, teal) and tumor weight (Fig. 6K), compared with GC chemotherapy treatment alone. Notably, we observed a decrease in fibrillar  $\text{Col3}$  staining in the stroma and number of  $\text{CD44}^{\text{high}}$  cancer cells in xenografts cotreated with VX-765 (Fig. 6, L and M). The VX-765 only arm did not significantly affect  $\text{CD44}^{\text{high}}$  cancer cells compared to the Veh group (fig. S7D). The combination of VX-765 with GC chemotherapy significantly suppressed iCAFs and hybrid i/myCAFs in the xenografts (fig. S7, E and F). Together, these findings establish that Casp1-mediated pyroptosis in response to chemotherapy modulates a fibrillar  $\text{Col3}$ -rich niche, favoring  $\text{CD44}^{\text{high}}$  CSCs.

### DISCUSSION

Most studies investigating chemotherapeutic response focus on optimizing the direct cytotoxic effects of chemotherapy to induce programmed cell death in cancer cells (45). Emerging studies revealed that cell death might not be the ultimate therapeutic endpoint, since certain types of lytic cell death are thought to be inflammatory and exert antitumoral properties via stimulating immune cell activities. Recently, a form of lytic cell death known as ferroptosis and its role in mediating antitumor or protumor function are under heavy scrutiny (46, 47). However, another form of lytic cell death—i.e., canonical Casp1-dependent pyroptosis—and its roles in cancer biology and therapy response are less studied. Canonical pyroptosis is thought to be inflammatory and primarily studied in relation to pathogenic infections in innate immune cells such as macrophages (48). Although some suggest that drug-induced pyroptosis functions as an immunogenic cell death with antitumor effects, these claims primarily focus on its effects on immune cells within the TME, often neglecting fibroblasts, which are a predominant cell type in the TME. In the current study, we show that chemotherapy induces Casp1-dependent pyroptosis in cancer cells, which promotes the release of several inflammatory chemokines, e.g., *CCL20*. This cell death modality facilitates the conversion of  $\alpha\text{SMA}^+$  CAFs into iCAFs in a *CCR6*-dependent manner. This is clinically relevant because a fibroblast gene signature driven by iCAF markers and collagen type III is associated with chemoresistance in bladder cancer. Contrary to current beliefs, iCAFs, rather than myCAFs, were found to produce collagen in the context of chemotherapy, thereby supporting the expansion of CSCs. In summary, these findings are noteworthy to challenge the prevailing notion that lytic or pyroptotic cell death is universally beneficial for anticancer therapy. Instead, our findings confirm that Casp1-dependent pyroptosis is inflammatory but engages inflammatory iCAFs to initiate a pyroptosis-iCAF-CSCs feedforward loop that drives chemoresistance in bladder cancer. Pharmaceutical inhibition of Casp1 sensitizes bladder cancer xenografts synergistically

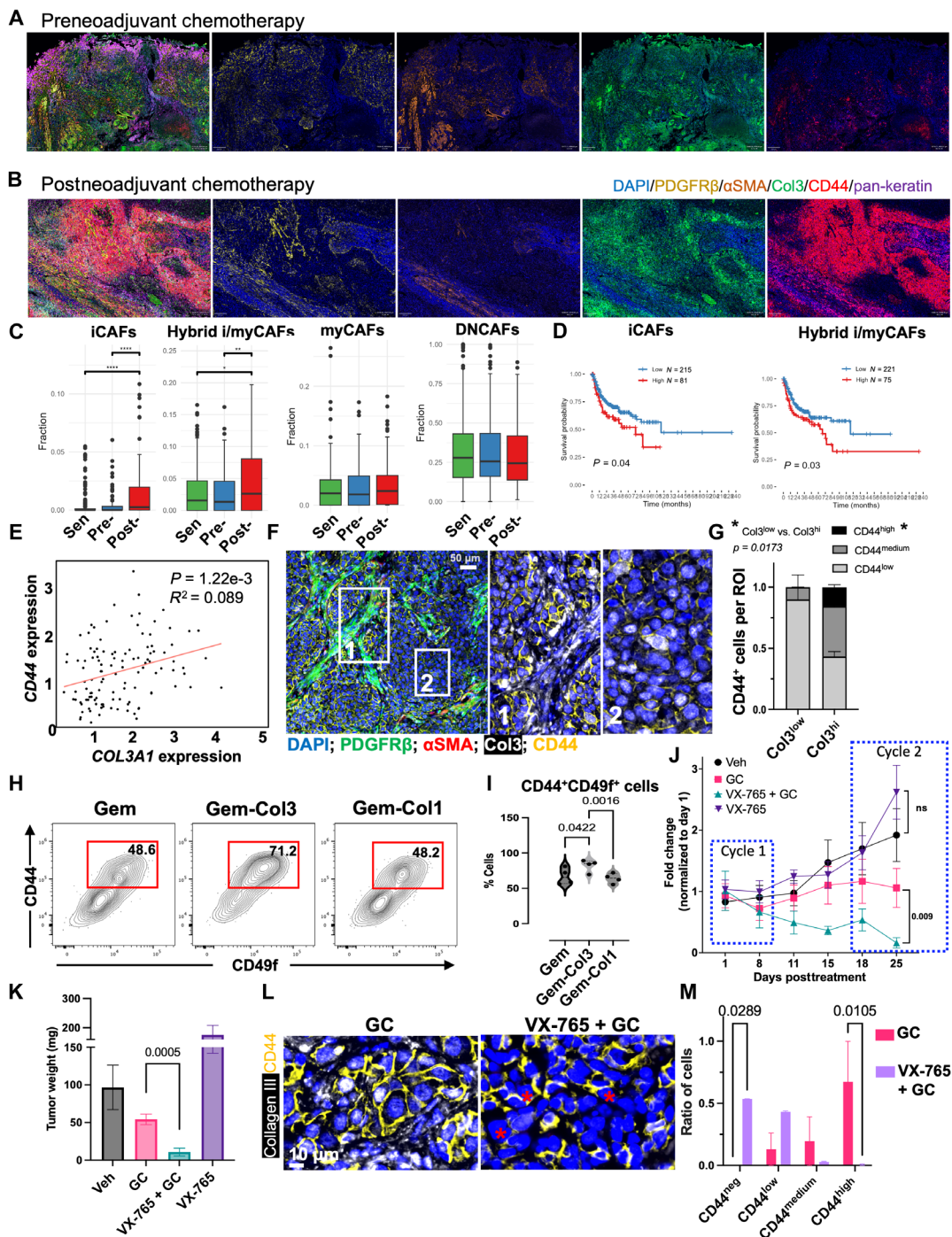


**Fig. 6. Pharmaceutical inhibition of Caspase 1 improves chemotherapy response.** (A and B) mIHC staining demonstrating iCAFs ( $\alpha$ SMA<sup>+</sup>PDGFR $\beta$ <sup>+</sup> CAFs) and CSCs (CD44<sup>+</sup>) in chemoresistant bladder cancer and association of Col3 with CD44<sup>+</sup> CSCs. (C) Bar graphs showing a significant elevation of digitally deconvoluted iCAFs and hybrid i/myCAFs in chemoresistant cohorts (GSE87304 and GSE124305) (\*\*\*\* $P < 0.0001$ ; \*\* $P < 0.01$ ; \* $P < 0.05$ ). (D) Kaplan-Meier analysis indicating worse survival in patients with high iCAFs or hybrid i/myCAFs (red) versus low expression (blue). (E) Scatterplot illustrating a positive correlation of COL3A1 with CD44 in patients with chemoresistant bladder cancer ( $P = 1.22 \times 10^{-3}$ ). (F) mIHC staining characterizing colocalization of PDGFR $\beta$  (green),  $\alpha$ SMA (red), Col3 (white), and CD44 (yellow) in bladder cancer xenografts, illustrating CD44<sup>high</sup> bladder cancer cells near Col3-rich stroma (region 1), and CD44<sup>medium</sup> or CD44<sup>low</sup> bladder cancer cells farther from Col3 area (region 2). (G) Bar graph quantifying the distribution of CD44<sup>high/med/low</sup> bladder cancer cells and their proximity to stromal Col3 staining, illustrating that CD44<sup>high</sup> and CD44<sup>med</sup> cancer cells are in a significantly higher percentage that is closely proximal to Col3-rich stromal areas. ROI, region of interest. (H and I) Flow cytometry assessing the effects of exogenous Col3 or collagen I (Col1) with gemcitabine on CD44<sup>+</sup>CD49f<sup>+</sup> CSCs and CD44<sup>-</sup>CD49f<sup>-</sup> differentiated cancer subpopulations. (J and K) Tumor size (J) and weight (K) of WT T24 xenografts upon GC chemotherapy in the presence or absence of Casp1 inhibitor VX-765, showing that VX-765 significantly improves chemosensitivity. (L and M) mIHC staining and quantification of Col3 and CD44 in GC versus VX-765 + GC xenografts. \* denoted that the cells were CD44<sup>-</sup> cancer cells in VX-765 + GC xenografts. VX-765 with GC reduces Col3 regions and CD44<sup>high</sup> cancer cells.

with chemotherapy, posing an attractive therapeutic strategy to be further evaluated (Fig. 7).

Cisplatin-based neoadjuvant chemotherapy (NAC) is the standard of care for locally invasive bladder cancer before radical cystectomy; however, meta-analysis of >3000 patients from 11 trials revealed that cisplatin-based chemotherapy provided a limited clinical benefit in improving ~5% of overall survival (28, 49). Tumor cell-intrinsic mechanisms, including DNA damage response and repair genes, e.g., ATM and ERCC2, are shown to associate with good response to chemotherapy (50–52). However, tumor cell-extrinsic mechanisms and the contribution of the bladder TME, such as stromal fibroblasts, to chemoresistance remain underexplored (13). Recently, analysis of patients with bladder cancer using scRNA-seq had revealed that CAF heterogeneity exists in bladder cancer, namely, myCAFs and iCAFs (24), as well as interferon-regulated CAFs (irCAFs) (19). However, how these CAF subtypes are regulated during a chemotherapy treatment context remains a research gap. Our findings revealed that patients with bladder cancer showing the enrichment of iCAF markers such as *IL-6* and *PDGFRB* could only gain limited benefit from NAC. Further, studies are only beginning to investigate the underlying mechanisms regulating CAF subtype conversion. Therefore, isolation of MIBC patient-derived primary CAFs provided a unique opportunity to microscopically observe and perform functional studies on these CAFs and their cross-talk with cancer cells, using clinical regimens of chemotherapy treatment.

Most functional studies assume that human CAFs are homogeneous  $\alpha\text{SMA}^{+/\text{high}}$  cell populations in monolayer culture in vitro; our current study revealed that a high heterogeneity of bladder CAF subtypes exists under distinct culture conditions (e.g., monolayer or coculture) and that these CAF subtype content changes rapidly in coculture with cancer cells and in chemotherapy treatment

conditions, which recapitulate the clinical scenario. Using multicolor flow cytometry and FlowSOM analysis, we identified 15 clusters of human bladder CAF subtypes, although such heterogeneity of CAFs was gradually lost during longer-term monolayer culture on a plastic surface, as the majority become  $\alpha\text{SMA}^{+}$  fibroblasts. Moreover, most of these  $\alpha\text{SMA}^{+}$  CAFs are considered as  $\alpha\text{SMA}^{+}\text{IL-6}^{+}\text{PDGFR}\beta^{+}$  hybrid i/myCAFs rather than the pure  $\alpha\text{SMA}^{+}\text{IL-6}^{-}\text{PDGFR}\beta^{-}$  myCAFs as previously assumed, and there remain a small  $\alpha\text{SMA}^{\text{low}/-}$  CAF subpopulation when analyzed and tracked by multicolor flow cytometry. When CAFs are cocultured with cancer cells in the chemotherapy context, there is a notable reduction in  $\alpha\text{SMA}^{+}$  CAFs, which is accompanied by an increase in  $\alpha\text{SMA}^{\text{low}}\text{IL-6}^{+}\text{PDGFR}\beta^{+}$  iCAFs—recapitulating the clinical scenario. During coculture, these iCAFs and hybrid CAFs respond to chemotherapy insult by producing Col3, initiating a vicious iCAF-to-CSC feedforward loop that likely contributes to the development of chemoresistance. The heterogeneity and dynamic changes in CAFs in response to chemotherapy and coculture would have been overlooked without the routine use of multicolor flow cytometry and/or multiplex IF staining in our study. Furthermore, this assay also enabled us to identify the  $\alpha\text{SMA}^{\text{low}}\text{IL-6}^{+}\text{PDGFR}\beta^{+}$  iCAFs and  $\alpha\text{SMA}^{+}\text{IL-6}^{+}\text{PDGFR}\beta^{+}$  hybrid i/myCAF, confirming that IL-6 can be expressed in iCAFs (21) as well as  $\alpha\text{SMA}^{+}$  CAFs (23), as previously observed but thought to be a contradictory finding by many in the field. Therefore, we propose that this multicolor flow cytometry is not only useful in providing new information to resolve existing controversy in the CAF field but should also be considered as a gold standard for assessing CAF heterogeneity in future research.

Another intriguing finding in the current study is the mechanistic connection between the emergence of inflammatory iCAFs and Casp1-mediated tumor cell pyroptosis, a type of inflammatory cell death (3). In an effort to uncover a potential effector from

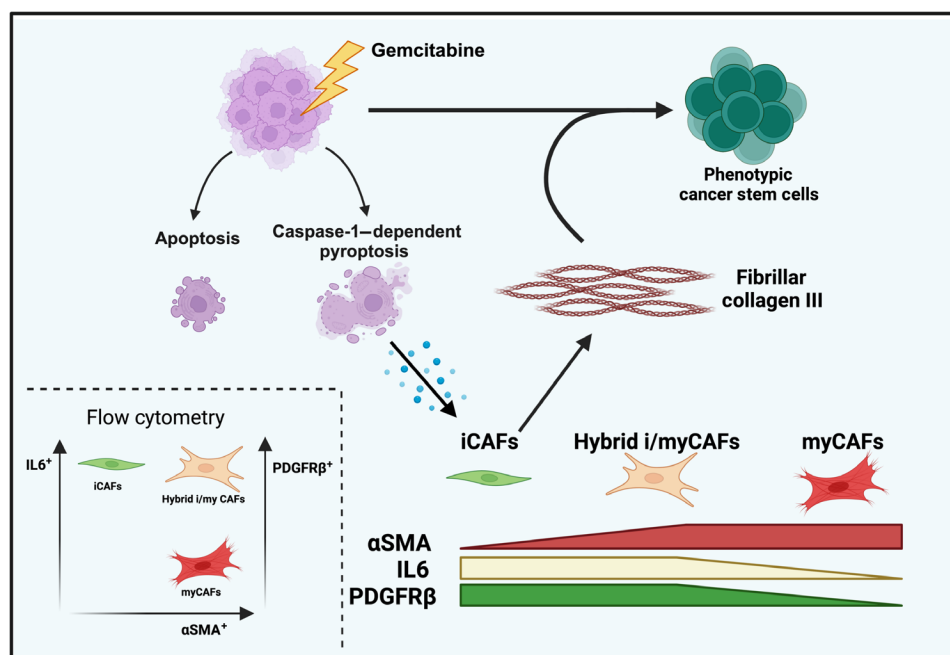


**Fig. 7. Schematic summarizing the overall conceptual advance.** Casp1-dependent tumor cell pyroptosis converts  $\alpha\text{SMA}^{\text{high}/+}$  myCAFs and  $\alpha\text{SMA}^{\text{high}/+}\text{PDGFR}\beta^{+}$  hybrid i/my CAFs into  $\alpha\text{SMA}^{\text{low}/-}\text{PDGFR}\beta^{+}$  collagen-III<sup>high</sup> iCAFs, which facilitates a feedforward loop fueling CSC expansion in patients with chemoresistant bladder cancer.

pyroptotic cancer cells that promotes iCAF expansion during chemotherapy, we identified a previously undescribed gemcitabine-induced, Casp1-dependent secretome. This secretome revealed a panel of paracrine molecules beyond the canonical Casp1 substrates, which may play a role in regulating CAF heterogeneity and influencing other cell types within the local TME. CCR6 inhibition was able to reduce iCAF population, alluding to a potential role of a CCR6-dependent signaling axis in expanding iCAFs that negatively affect chemotherapy treatment outcomes.

During pathogenic infections, pyroptosis acts as a natural inflammatory response and is a critical host defense mechanism (7). However, in the context of chemotherapy-induced tumor pyroptosis, its role remains uncharacterized (2). Although pyroptosis is widely accepted to exert antitumoral activities in treatment-naïve condition, most studies highlight the antitumoral roles of caspase-1 independent pyroptosis, particularly through the cleavage and activation of gasdermin family proteins (53). Therefore, it remains to be further investigated how pyroptotic-inducing or pyroptotic inhibitory agents might synergize with chemotherapy or other conventional therapies across various cancer types, and how noncanonical pyroptosis pathway might affect cancer biology in a broader context representing an exciting research area of ongoing development.

## MATERIALS AND METHODS

### Cell culture

Cell culture was conducted under standard conditions (i.e., 5% CO<sub>2</sub>, 37°C). The human bladder cancer cell line T24 was obtained from American Type Culture Collection (ATCC) and maintained in DMEM high-glucose medium supplemented with 10% FBS (Gen-Depot, F0900-050, v/v) as previously described (26, 27, 54). Casp1 KO T24 cells were generated using CRISPR-Cas9 gene editing via electroporation, and guide RNA sequence was TATCCTTT-GAGCTTCTTCTA. CAFs were cultured in DMEM/F12 medium (Thermo Fisher Scientific, 11320082) supplemented with 20% FBS (v/v), detached by TrypLE (Gibco, 12605-028) and centrifuged at 100g for 10 min. Low passages of CAFs (four to eight passages) were used for experiments. All media were supplemented with streptomycin (100 µg/ml) and penicillin (100 U/ml; Thermo Fisher Scientific, 15140163). Cell culture is routinely monitored for mycoplasma using the MycoAlert Detection Kit (Lonza, LT07-318).

Primary CAFs were isolated from muscle-invasive bladder carcinoma samples, which were obtained during cyst section. The sheared tissues (~1 mm<sup>3</sup>) were digested with collagenase II (Thermo Fisher Scientific, 17101015) and deoxyribonuclease I (Sigma-Aldrich, 11284932001) in DMEM with 10% FBS and penicillin-streptomycin at 37°C for 30 to 45 min. The cells were collected by centrifugation at 380g for 5 min and filtered through 40-µm cell strainers. The cells were implanted in Matrigel for organoid expansion, and the fibroblasts were attached to a plastic surface. The attached fibroblasts were expanded in the dish with DMEM-F12 with 20% FBS and penicillin-streptomycin after the removal of organoid Matrigel domes. The expanded CAFs were validated by FACS with similar expression levels of EpCAM, CD31, and CD45 as normal bladder fibroblasts purchased from ATCC (PCS-420-013).

### In vitro drug treatment

Cells were treated with gemcitabine [Chemical Abstracts Service Registry Number (CAS)# 122111-03-9, TCI America] in 2% FBS

DMEM medium for 48 hours, and postchemotherapy cells were replenished with fresh 2% FBS DMEM medium for 4 days of repopulation phase. The IC<sub>50</sub> of gemcitabine for T24 and CAFs was determined by quantifying DAPI<sup>+</sup> cells via flow cytometry. CM was collected from vehicle or 0.5 µM gemcitabine-treated T24 cells at 48 hours.

The subpopulations of CAFs were analyzed after 8 days of exposure to CM. Cytokine/chemokine inhibitors were prepared according to the manufacturer's instructions and dissolved in CM from 48 hours of gemcitabine-treated WT T24 cells, CXCR2 Ab (MAB331-100, R&D) at 2 µg/µl, CXCL10 Ab (MAB266-100, R&D) at 2 µg/µl, CCL20 Ab (ab9829, Abcam) at 10 µg/µl, and CCR6i (HY-112701, MedChemExpress) at 10 µg/µl. CM with/without inhibitors was replenished every 2 days.

### Cytokine Ab arrays

The Human XL Cytokine Array Kit (ARY022B, R&D) was used according to the manufacturer's protocol. Briefly, 1.5 ml of a mixture of culture medium and assay buffer was incubated with the membrane on a rocking platform overnight at 4°C, followed by 1-hour incubation with the detection Ab cocktail. The signal was detected with chemiluminescence using Bio-Rad Chemidoc. The data were analyzed using Image Lab Software.

### Enzyme-linked immunosorbent assay

The concentrations of CXCL5, CXCL10, and CCL20 from gemcitabine-treated T24 cells were measured using ELISA kits and were conducted according to the manufacturer's protocols: human CXCL5 DuoSet ELISA (DY254-05, R&D), human CXCL10/IP-10 DuoSet ELISA (DY266-05, R&D), human CCL20/MIP-3 alpha DuoSet ELISA (DY360-05, R&D).

### Flow cytometry

The analysis of CAF heterogeneity in vitro was conducted using multiplex staining and flow cytometry. Briefly, cells at the end of the designed time point were washed with phosphate-buffered saline (PBS) and trypsinized using TrypLE for 10 min. The suspended cells were washed by 10% FBS DMEM and prechilled 2% FBS PBS. The cells were stained with Fixable Violet dye for 10 min in PBS followed by surface marker staining diluted in the brilliant buffer (566349, BD Biosciences) for 30 min on ice. After washed with 2% FBS PBS two times and spanned down at 600g for 5 min, cells were fixed in 200 µl of fixation buffer (BDB554722) on ice for 20 min and subsequently permeabilized by 1× permeabilization buffer (Invitrogen, 00-8333-56) for 10 min. Intracellular Abs were diluted in a 1× permeabilization buffer, and cells were stained for 30 min on ice. The samples were suspended in flow cytometry (FACS) buffer, 2% (w/v) bovine serum albumin, 2 mM EDTA, and 25 mM Hepes and subjected to a Cytek analyzer. Data analysis was performed in FlowJo software (BD Biosciences).

For apoptosis assay, the suspended cells were stained with CD13-phycoerythrin (PE)/Cyanine7 (Cy7), CD44-fluorescein isothiocyanate (FITC), and CD49f-PerCP/Cy5.5 in 2% FBS PBS for 30 min and washed with 2% FBS PBS buffer for one time. The cells were washed in 1× binding buffer (556454, BD Biosciences) for one time and stained with annexin V-APC (1:100; 550474, BD Biosciences) in 1× binding buffer for 15 min. The samples were suspended in a DAPI-contained (0.1 mg/liter) 1× binding buffer and analyzed in a Cytek analyzer or BD Fortessa.

For cell sorting, the samples were stained with CD13-PE/Cy7, PDGFR $\beta$ -PE, and FAP-FITC in 2% FBS for 30 min and followed by two times of washing. The cells were suspended in DAPI (0.5 mg/liter) FACS buffer and sorted in BD FACARIA. Unstained and single stained compensation beads (Thermo Fisher Scientific, 50-112-9040) were used for compensation.

### Multispectral imaging of multiplex-stained tissue sections

The mxIHC procedures followed the protocol published before (27). Briefly, paraffin-embedded T24 xenografts were sectioned at 5  $\mu$ m. Sections were incubated at 65°C for 1 hour and then treated with xylene (2  $\times$  5 min), 100% ethanol (2  $\times$  50 dips), 95% ethanol (2  $\times$  50 dips), 70% ethanol (2  $\times$  50 dips), and H<sub>2</sub>O for 50 dips. Sections were incubated in 10% formalin for 20 min and washed with TBST. Antigen retrieval was performed by steaming in 1 $\times$  antigen retrieval buffer (pH 9) (ab93684, Abcam) for 25 min. After the sections cooling down, sections were blocked with 1 $\times$  animal-free buffer [15019L, Cell Signaling Technology (CST)] for 10 min and incubated with the Abs diluted in the optimized concentration (table S2). The sections were washed three times in TBST and incubated in the matched secondary Abs (table S3) for 30 min followed by three times of TBST wash. Sections were blocked with Opal fluorophores (table S4) diluted in amplification buffer (FP1498, Akoya) for 10 min, and washed three times in TBST. Antigen retrieval in 1 $\times$  citrate buffer (C9999-1000ML, Sigma-Aldrich) was applied to wash off the previous Abs between each round of staining. After the last marker staining, the sections were incubated with DAPI in TBST (2  $\mu$ g/ml) for 5 min, followed by three times of washing, and mounted with ProLong Gold Antifade Reagent with DAPI (P36935, Invitrogen).

Slides were scanned by Phenocycler Fusion (Akoya Biosciences), spectral unmixing was applied in PhenoChart and inForm, and cell segmentation was performed in QuPath. Each section was scanned in its entirety by using  $\times$ 20 or  $\times$ 40 magnification.

### Reverse transcription PCR

Isolation of mRNA from cells was performed using the RNAqueous Micro Kit (Invitrogen, AM1931), followed by reverse transcription with the iScript cDNA Synthesis Kit (Bio-Rad, 170-8891). Quantitative real-time reverse transcription PCR was conducted using iTaq Universal SYBR Green Supermix (Bio-Rad, 172-5121) and a Roche Light Cycler 96 machine. Primers used are listed in table S5.

### SDS–polyacrylamide gel electrophoresis and Western blotting

T24 bladder cancer cells were seeded at a density of 3  $\times$  10<sup>4</sup> cells/cm<sup>2</sup>. For in vitro analysis of chemotherapy treatment, cells were treated the next day at either IC<sub>50</sub> dosage of gemcitabine or control in DMEM high glucose supplemented with 2% (v/v) FBS. Following the time point as described in Results, the supernatant was collected and centrifuged at 1200g  $\times$  5 min at 4°C, while the cells were lysed in ice-cold radioimmunoprecipitation assay buffer (Thermo Fisher Scientific) supplemented with 1 $\times$  protease and phosphatase inhibitors (Roche). Cell lysates were then combined with the pellet from their corresponding supernatant to include dying cell fractions. Following lysis on ice, samples were cleared at >12,000 rpm for 20 min at 4°C. Protein concentrations were quantified using the BCA assay (Thermo Fisher Scientific). SDS–polyacrylamide gel electrophoresis was run loading equal mass into various percentage polyacrylamide gels and transferred onto 0.45- or 0.2- $\mu$ m polyvinylidene difluoride

(Sigma-Aldrich). After blocking, the membranes were incubated in the following primary Abs overnight: Casp1 (1:1000; CST, #2423S), Casp3 (1:1000; CST, #9662), PARP (1:1000; CST, #9542),  $\beta$ -actin (1:2000; Santa Cruz, sc-47778), and glyceraldehyde phosphate dehydrogenase (1:2000; CST, #2118). Membranes were subsequently probed with respective the host-conjugated horseradish peroxidase (HRP) secondary Ab (1:10,000) and imaged on Chemi-Doc (Bio-Rad).

### Xenograft tumor growth

Animal work was performed according to ethical regulations approved by Houston Methodist Research Institute IACUC #IS00007158. Four-week-old male C;129S4-Rag2<sup>tm1.1Flv</sup>Il2rg<sup>tm1.1Flv</sup>/J mice were purchased from the Jackson Laboratory and were housed in the individually ventilated cages in Houston Methodist Research Institute, comparative medicine facility. Room lighting was set to a 12-hour light-dark cycle. Water and regular chow diet were provided to animals, ad libitum.

For xenograft studies, 1 million T24 WT or Casp1 KO cells mixed with Matrigel were inoculated in the left and right flanks subcutaneously. When the tumor size reached to a palpable size, mice were randomized into different experimental groups: vehicle control, chemotherapy treatment group, and with or without VX-765 (Belnacasan) cotreatment. For systemic administration of GC treatment, mice were sequentially intraperitoneally injected with gemcitabine (60 mg/kg; CAS# 122111-03-9, TCI America) and cisplatin (6 mg/kg; CAS# 15663-27-1, Sigma-Aldrich) at day 1, followed by gemcitabine single treatment at day 8 to complete 1 cycle of treatment. Mice were given 1 week of drug holiday before administering the second cycle of treatment. For VX-765 (50 mg/kg; Belnacasan, CAS# 273404-37-8, MedChemExpress) treatment, mice were dosed twice a week upon the start of the first cycle of chemotherapy until the scientific endpoint of experiment.

### The bladder scRNA-seq datasets and fibroblast identification

The scRNA-seq datasets for bladder cancer presented here were downloaded from the National Center for Biotechnology Information Gene Expression Omnibus (GSE146137, GSE192575, and GSE130001), which included a total of six patient datasets. The following study was downloaded from the Mendeley database (Mendeley at DOI 10.17632/7yb7s9769c.1) also included six patient datasets. In addition to these, data from 25 patients were downloaded from Gene Expression Omnibus database (GSE169379) in h5ad format and were converted to h5seurat format using SeuratDisk package (version 0.0.0.9021). All these datasets were processed, filtered, and clustered separately. For filtering, the following parameters were applied: nUMI  $\geq$  400, nGene  $\geq$  250, log10GenesPerUMI > 0.8, and mitoRatio < 0.2. Data were then normalized with NormalizeData function, and the 2000 most variable features were then identified to find variable features. Data were scaled before SCTransform, and principal components analysis was performed. To normalize the batch effect, the Harmony package (version 0.1.1) was used before clustering. The dimensionality of the dataset was assessed using the t-distributed stochastic neighbor embedding (tSNE) method. Clusters were calculated, and data dimensions were reduced using the UMAP method. Cell types within each cluster defined by pre-defined gene expressions such as “KRT5,” “EPCAM,” and “CDH1” are used for epithelial cells; “FAP,” “PDPN,” “ACTA2,” and “COL1A1” are for fibroblast (CAFs); “CD3E,” “CD4,” “CD8A,” and “FOXP3” are

for T cells; and “*S100A9*,” “*S100A8*,” “*CD74*,” “*MRC1*,” “*CX3CR1*,” “*LYZ*,” “*CSF1R*,” “*ITGAM*,” and “*ITGAX*” for myeloid lineage. In addition to this, the top differentially expressed genes were examined for each cluster relative to all other clusters using the Seurat FindAllMarkers function (test used: Wilcox or MAST). Predefined fibroblast (CAF) clusters were subsetted using Seurat:subset function, and previous steps including SCTransform and Harmony normalization were applied. Clusters that contained gene markers that are associated with endothelial cells (PLVAP<sup>+</sup>PECAM1<sup>+</sup>), pericytes (RGS5<sup>+</sup>MCAM<sup>+</sup>) or uncharacterized/noncoding transcripts were removed, and the remaining clusters were reclustered and categorized into four CAF types based on their mean *ACTA2* and *IL6* expression (myCAF, hybrid, iCAF, and DNCAF).

### CAF type deconvolution analysis

Public patient datasets (GSE87304 and GSE124305) with survival and gene expression data were subject to digital deconvolution using Estimating the Proportions of Immune and Cancer cells (EPIC) R package. Briefly, the reference matrix was prepared using the fibroblast Seurat object rendered from the bladder cancer patient samples. The matrix used the top 20 marker genes from the myCAF, hybrid, iCAF, and DNCAF clusters. The cellFractions part of the EPIC output was used to compare the proportions of different CAFs in each patient sample. The statistical significance of CAF proportion and survival difference between different patient groups were determined using Wilcoxon's test and log-rank test, respectively, with an  $\alpha$  of 0.05. The output graphs were plotted using ggplot2, ggsurvplot, ggsignif, and survminer packages.

### Transcriptomic dataset analyses

Gene expression profiles from bulk RNA-seq of 113 patients, along with clinical and survival data, pre- (GSE87304) and postneoadjuvant (GSE124305) cisplatin-based chemotherapy were retrieved from Gene Expression Omnibus. The expression levels of CAF markers (*ACTA2*, *IL6*, *PDGFRB*, and *COL3A1*) were normalized and scaled for heatmap plotting. Clustering was performed using the Euclidean distance method. Significant differences between the overall survival of patients in the two major clusters were assessed using the log-rank test with an  $\alpha = 0.05$ . The expression differences of *CASP1* and *ACTA2* between pre-/posttreatment and clusters were assessed by pairwise Student's *t* test, with *P* values adjusted using the Bonferroni method ( $\alpha = 0.05$ ). The linear correlation between the expression of *CD44* and *COL3A1* under various conditions was tested using a *t* test ( $\alpha = 0.05$ ) and Pearson's correlation coefficient.

### Statistics

All experiments were performed in at least three biological replicates. Data for descriptive statistics are expressed as SEM, unless otherwise specified. Statistical analysis and graphs were performed using GraphPad Prism (v.10). Analysis of variance (ANOVA) was applied to identify variation between groups, followed by multiple comparisons among groups (two-tailed *t* tests, Sidak assay, multiple Mann-Whitney tests, etc.). *P* < 0.05 was considered to be statistically significant.

### Supplementary Materials

This PDF file includes:

Figs. S1 to S7

Tables S1 to S5

### REFERENCES AND NOTES

1. M. Lamkanfi, V. M. Dixit, Mechanisms and functions of inflammasomes. *Cell* **157**, 1013–1022 (2014).
2. J. Hou, J. M. Hsu, M. C. Hung, Molecular mechanisms and functions of pyroptosis in inflammation and antitumor immunity. *Mol. Cell* **81**, 4579–4590 (2021).
3. J. Shi, Y. Zhao, K. Wang, X. Shi, Y. Wang, H. Huang, Y. Zhuang, T. Cai, F. Wang, F. Shao, Cleavage of GSDMD by inflammatory caspases determines pyroptotic cell death. *Nature* **526**, 660–665 (2015).
4. L. Galluzzi, I. Vitale, S. A. Aaronson, J. M. Abrams, D. Adam, P. Agostinis, E. S. Alnemri, L. Altucci, I. Amelio, D. W. Andrews, M. Annicchiarico-Petruzzelli, A. V. Antonov, E. Arama, E. H. Baehrecke, N. A. Barlev, N. G. Bazan, F. Bernassola, M. J. M. Bertrand, K. Bianchi, M. V. Blagosklonny, K. Blomgren, C. Borner, P. Boya, C. Brenner, M. Campanella, E. Candi, D. Carmona-Gutierrez, F. Cecconi, F. K.-M. Chan, N. S. Chandel, E. H. Cheng, J. E. Chipuk, J. A. Cidlowski, A. Ciechanover, G. M. Cohen, M. Conrad, J. R. Cubillos-Ruiz, P. E. Czabotar, V. D'Angiolella, T. M. Dawson, V. L. Dawson, V. De Laurenzi, R. De Maria, K.-M. Debatin, R. J. De Berardinis, M. Deshmukh, N. D. Daniele, F. D. Virgilio, V. M. Dixit, S. J. Dixon, C. S. Duckett, B. D. Dynlacht, W. S. El-Deiry, J. W. Elrod, G. M. Fimia, S. Fulda, A. J. Garcia-Sáez, A. D. Garg, C. Garrido, E. Gavathiotis, P. Golstein, E. Gottlieb, D. R. Green, L. A. Greene, H. Gronemeyer, A. Gross, G. Hajnoczky, J. M. Hardwick, I. S. Harriss, M. O. Hengartner, C. Hetz, H. Ichijo, M. Jäättelä, B. Joseph, P. J. Jost, P. P. Juin, W. J. Kaiser, M. Karin, T. Kaufmann, O. Kepp, A. Kimchi, R. N. Kitsis, D. J. Klionsky, R. A. Knight, S. Kumar, S. W. Lee, J. J. Lemasters, B. Levine, A. Linkermann, S. A. Lipton, R. A. Lockshin, C. López-Otin, S. W. Lowe, T. Luedde, E. Lugli, M. M. Farlane, M. Madeo, M. Malewicz, W. Malorni, G. Manic, J.-C. Marine, S. J. Martin, J.-C. Martinou, J. P. Medema, P. Mehlen, P. Meier, S. Melino, E. A. Miao, J. D. Molkenin, U. M. Moll, C. Muñoz-Pinedo, S. Nagata, G. Nuñez, A. Oberst, M. Oren, M. Overholtzer, M. Pagano, T. Panaretakis, M. Pasparakis, J. M. Penninger, D. M. Pereira, S. Pervaiz, M. E. Peter, M. Piacentini, P. Pinton, J. H. M. Prehn, H. Puthalakath, G. A. Rabinovich, M. Rehm, R. Rizzuto, C. M. P. Rodrigues, D. C. Rubinsztein, T. Rudel, K. M. Ryan, E. Sayan, L. Scorrano, F. Shao, Y. Shi, J. Silke, H.-U. Simon, A. Sistigu, B. R. Stockwell, A. Strasser, G. Szabadkai, S. W. G. Tait, D. Tang, N. Tavernarakis, A. Thorburn, Y. Tsujimoto, B. Turk, T. V. Berghe, P. Vandenabeele, M. G. Vander Heiden, A. Villunger, H. W. Virgin, K. H. Vousden, D. Vucic, E. F. Wagner, H. Walczak, D. Wallach, Y. Wang, J. A. Wells, W. Wood, J. Yuan, Z. Zakeri, B. Zhivotovskiy, L. Zitvogel, G. Melino, G. Kroemer, Molecular mechanisms of cell death: Recommendations of the Nomenclature Committee on Cell Death 2018. *Cell Death Differ.* **25**, 486–541 (2018).
5. K. Newton, A. Strasser, N. Kayagaki, V. M. Dixit, Cell death. *Cell* **187**, 235–256 (2024).
6. R. Miao, C. Jiang, W. Y. Chang, H. Zhang, J. An, F. Ho, P. Chen, H. Zhang, C. Junqueira, D. Amgalan, F. G. Liang, J. Zhang, C. L. Evavold, I. Hafner-Bratkovič, Z. Zhang, P. Fontana, S. Xia, M. Waldeck-Weiermair, Y. Pan, T. Michel, L. Bar-Peled, H. Wu, J. C. Kagan, R. N. Kitsis, P. Zhang, X. Liu, J. Lieberman, Gasdermin D permeabilization of mitochondrial inner and outer membranes accelerates and enhances pyroptosis. *Immunity* **56**, 2523–2541.e8 (2023).
7. T. Bergsbaken, S. L. Fink, B. T. Cookson, Pyroptosis: Host cell death and inflammation. *Nat. Rev. Microbiol.* **7**, 99–109 (2009).
8. F. S. Younesi, A. E. Miller, T. H. Barker, F. M. V. Rossi, B. Hinz, Fibroblast and myofibroblast activation in normal tissue repair and fibrosis. *Nat. Rev. Mol. Cell Biol.* **25**, 617–638 (2024).
9. M. Tsoumakidou, The advent of immune stimulating CAFs in cancer. *Nat. Rev. Cancer* **23**, 258–269 (2023).
10. Y. A. DeClerck, Desmoplasia: A response or a niche? *Cancer Discov.* **2**, 772–774 (2012).
11. A. Velez-Delgado, K. L. Donahue, K. L. Brown, W. Du, V. Irizarry-Negron, R. E. Menjivar, E. L. Lasse Opsahl, N. G. Steele, S. The, J. Lazarus, V. R. Siritirachai, W. Yan, S. B. Kemp, S. A. Kerk, M. Bollampally, S. Yang, M. K. Scales, F. R. Avritt, F. Lima, C. A. Lyssiotis, A. Rao, H. C. Crawford, F. Bednar, T. L. Frankel, B. L. Allen, Y. Zhang, M. Pasca di Magliano, Extrinsic KRAS signaling shapes the pancreatic microenvironment through fibroblast reprogramming. *Cell Mol. Gastroenterol. Hepatol.* **13**, 1673–1699 (2022).
12. R. Kalluri, The biology and function of fibroblasts in cancer. *Nat. Rev. Cancer* **16**, 582–598 (2016).
13. Y. C. Lee, H. M. Lam, C. Rosser, D. Theodorescu, W. C. Parks, K. S. Chan, The dynamic roles of the bladder tumour microenvironment. *Nat. Rev. Urol.* **19**, 515–533 (2022).
14. C. Liu, M. Mak, Fibroblast-mediated uncaging of cancer cells and dynamic evolution of the physical microenvironment. *Sci. Rep.* **12**, 791 (2022).
15. P. Durning, S. L. Schor, R. A. Sellwood, Fibroblasts from patients with breast cancer show abnormal migratory behaviour in vitro. *Lancet* **2**, 890–892 (1984).
16. E. Elyada, M. Bolisetty, P. Laise, W. F. Flynn, E. T. Courtois, R. A. Burkhart, J. A. Teinor, P. Belleau, G. Biffi, M. S. Lucito, S. Sivajothi, T. D. Armstrong, D. D. Engle, K. H. Yu, Y. Hao, C. L. Wolfgang, Y. Park, J. Preall, E. M. Jaffee, A. Califano, P. Robson, D. A. Tuveson, Cross-species single-cell analysis of pancreatic ductal adenocarcinoma reveals antigen-presenting cancer-associated fibroblasts. *Cancer Discov.* **9**, 1102–1123 (2019).
17. E. Sahai, I. Atsaturov, E. Cukierman, D. G. DeNardo, M. Egeblad, R. M. Evans, D. Fearon, F. R. Greten, S. R. Hingorani, T. Hunter, R. O. Hynes, R. K. Jain, T. Janowitz, C. Jorgensen, A. C. Kimmelman, M. G. Kolonin, R. G. Maki, R. S. Powers, E. Pure, D. C. Ramirez,

- R. Scherz-Shouval, M. H. Sherman, S. Stewart, T. D. Tlsty, D. A. Tuveson, F. M. Watt, V. Weaver, A. T. Weeraratna, Z. Werb, A framework for advancing our understanding of cancer-associated fibroblasts. *Nat. Rev. Cancer* **20**, 174–186 (2020).
18. H. Hu, Z. Piotrowska, P. J. Hare, H. Chen, H. E. Mulvey, A. Mayfield, S. Noeen, K. Kattermann, M. Greenberg, A. Williams, A. K. Riley, J. J. Wilson, Y. Q. Mao, R. P. Huang, M. K. Banwait, J. Ho, G. S. Crowther, L. P. Hariri, R. S. Heist, D. P. Kodack, L. Pinello, A. T. Shaw, M. Mino-Kenudson, A. N. Hata, L. V. Sequist, C. H. Benes, M. J. Niederst, J. A. Engelman, Three subtypes of lung cancer fibroblasts define distinct therapeutic paradigms. *Cancer Cell* **39**, 1531–1547.e10 (2021).
  19. Z. Ma, X. Li, Y. Mao, C. Wei, Z. Huang, G. Li, J. Yin, X. Liang, Z. Liu, Interferon-dependent SLC14A1<sup>+</sup> cancer-associated fibroblasts promote cancer stemness via WNT5A in bladder cancer. *Cancer Cell* **40**, 1550–1565.e7 (2022).
  20. L. Cords, S. Engler, M. Haberecker, J. H. Ruschhoff, H. Moch, N. de Souza, B. Bodenmiller, Cancer-associated fibroblast phenotypes are associated with patient outcome in non-small cell lung cancer. *Cancer Cell* **42**, 396–412.e5 (2024).
  21. D. Ohlund, A. Handly-Santana, G. Biffi, E. Elyada, A. S. Almeida, M. Ponz-Sarvisé, V. Corbo, T. E. Oni, S. A. Hearn, E. J. Lee, I. I. C. Chio, C.-I. Hwang, H. Tiriác, L. A. Baker, D. D. Engle, C. Feig, A. Kulthi, M. Egeblad, D. T. Fearon, J. M. Crawford, H. Clevers, Y. Park, D. A. Tuveson, Distinct populations of inflammatory fibroblasts and myofibroblasts in pancreatic cancer. *J. Exp. Med.* **214**, 579–596 (2017).
  22. A. Costa, Y. Kieffer, A. Scholer-Dahirel, F. Pelon, B. Bourachot, M. Cardon, P. Sirven, I. Magagna, L. Fuhrmann, C. Bernard, C. Bonneau, M. Kondratova, I. Kuperstein, A. Zinovyev, A. M. Givel, M. C. Parrini, V. Soumelis, A. Vincent-Salomon, F. Mechta-Grigoriou, Fibroblast heterogeneity and immunosuppressive environment in human breast cancer. *Cancer Cell* **33**, 463–479.e10 (2018).
  23. K. M. McAndrews, Y. Chen, J. K. Darpolar, X. Zheng, S. Yang, J. L. Carstens, B. Li, H. Wang, T. Miyake, P. Correa de Sampaio, M. L. Kirtley, M. Natale, C. C. Wu, H. Sugimoto, V. S. LeBlau, R. Kalluri, Identification of functional heterogeneity of carcinoma-associated fibroblasts with distinct IL6-mediated therapy resistance in pancreatic cancer. *Cancer Discov.* **12**, 1580–1597 (2022).
  24. Z. Chen, L. Zhou, L. Liu, Y. Hou, M. Xiong, Y. Yang, J. Hu, K. Chen, Single-cell RNA sequencing highlights the role of inflammatory cancer-associated fibroblasts in bladder urothelial carcinoma. *Nat. Commun.* **11**, 5077 (2020).
  25. A. V. Kurtova, J. Xiao, Q. Mo, S. Pazhanisamy, R. Krasnow, S. P. Lerner, F. Chen, T. T. Roh, E. Lay, P. L. Ho, K. S. Chan, Blocking PGE2-induced tumour repopulation abrogates bladder cancer chemoresistance. *Nature* **517**, 209–213 (2015).
  26. K. Hayashi, F. Nikolos, Y. C. Lee, A. Jain, E. Tsoouko, H. Gao, A. Kasabyan, H. E. Leung, A. Osipov, S. Y. Jung, A. V. Kurtova, K. S. Chan, Tipping the immunostimulatory and inhibitory DAMP balance to harness immunogenic cell death. *Nat. Commun.* **11**, 6299 (2020).
  27. F. Nikolos, K. Hayashi, X. P. Hoi, M. E. Alonzo, Q. Mo, A. Kasabyan, H. Furuya, J. Trepel, D. Di Vizio, J. Guarnerio, D. Theodorescu, C. Rosser, A. Apolo, M. Galsky, K. S. Chan, Cell death-induced immunogenicity enhances chemioimmunotherapeutic response by converting immune-excluded into T-cell inflamed bladder tumors. *Nat. Commun.* **13**, 1487 (2022).
  28. Advanced Bladder Cancer (ABC) Meta-analysis Collaboration, Neoadjuvant chemotherapy in invasive bladder cancer: Update of a systematic review and meta-analysis of individual patient data advanced bladder cancer (ABC) meta-analysis collaboration. *Eur. Urol.* **48**, 202–206 (2005).
  29. W. Choi, S. Porten, S. Kim, D. Willis, E. R. Plimack, J. Hoffman-Censits, B. Roth, T. Cheng, M. Tran, I. L. Lee, J. Melquist, J. Bondaruk, T. Majewski, S. Zhang, S. Pretzsch, K. Baggerly, A. Siefkert-Radtke, B. Czerniak, C. P. Dinney, D. J. McConkey, Identification of distinct basal and luminal subtypes of muscle-invasive bladder cancer with different sensitivities to frontline chemotherapy. *Cancer Cell* **25**, 152–165 (2014).
  30. J. Racle, D. Gfeller, EPIC: A tool to estimate the proportions of different cell types from bulk gene expression data. *Methods Mol. Biol.* **2120**, 233–248 (2020).
  31. C. Shiau, J. Cao, D. Gong, M. T. Gregory, N. J. Caldwell, X. Yin, J. W. Cho, P. L. Wang, J. Su, S. Wang, J. W. Reeves, T. K. Kim, Y. Kim, J. A. Guo, N. A. Lester, J. W. Bae, R. Zhao, N. Schurman, J. L. Barth, M. L. Ganci, R. Weissleder, T. Jacks, M. Qadan, T. S. Hong, J. Y. Wo, H. Roberts, J. M. Beechem, C. F. Castillo, M. Mino-Kenudson, D. T. Ting, M. Hemberg, W. L. Hwang, Spatially resolved analysis of pancreatic cancer identifies therapy-associated remodeling of the tumor microenvironment. *Nat. Genet.* **56**, 2466–2478 (2024).
  32. H. Wang, Y. Mei, C. Luo, Q. Huang, Z. Wang, G. M. Lu, L. Qin, Z. Sun, C. W. Huang, Z. W. Yang, J. Chen, W. Yin, C. N. Qian, J. Zeng, L. Chen, Q. Leng, Y. Guo, G. Jia, Single-cell analyses reveal mechanisms of cancer stem cell maintenance and epithelial-mesenchymal transition in recurrent bladder cancer. *Clin. Cancer Res.* **27**, 6265–6278 (2021).
  33. J. A. Grout, P. Sirven, A. M. Leader, S. Maskey, E. Hector, I. Puisieux, F. Steffan, E. Cheng, N. Tung, M. Maurin, R. Vaineau, L. Karpf, M. Plaud, A. L. Begue, K. Ganesh, J. Mesple, M. Casanova-Acebes, A. Tabachnikova, S. Keerthivasan, A. Lansky, J. L. Berichel, L. Walker, A. H. Rahman, S. Gnajatic, N. Girard, M. Lefevre, D. Damotte, J. Adam, J. C. Martin, A. Wolf, R. M. Flores, M. B. Beasley, R. Pradhan, S. Muller, T. U. Marron, S. J. Turley, M. Merad, E. Kenigsberg, H. Salmon, Spatial positioning and matrix programs of cancer-associated fibroblasts promote T-cell exclusion in human lung tumors. *Cancer Discov.* **12**, 2606–2625 (2022).
  34. L. Cords, S. Tietscher, T. Anzener, C. Langwieder, M. Rees, N. de Souza, B. Bodenmiller, Cancer-associated fibroblast classification in single-cell and spatial proteomics data. *Nat. Commun.* **14**, 4294 (2023).
  35. H. van Splunder, P. Villacampa, A. Martinez-Romero, M. Graupera, Pericytes in the disease spotlight. *Trends Cell Biol.* **34**, 58–71 (2024).
  36. M. Bartoschek, N. Oskolkov, M. Bocci, J. Lovrot, C. Larsson, M. Sommarin, C. D. Madsen, D. Lindgren, G. Pekar, G. Karlsson, M. Ringner, J. Bergh, A. Björklund, K. Pietras, Spatially and functionally distinct subclasses of breast cancer-associated fibroblasts revealed by single cell RNA sequencing. *Nat. Commun.* **9**, 5150 (2018).
  37. W. Kim, D. A. Barron, R. San Martin, K. S. Chan, L. L. Tran, F. Yang, S. J. Ressler, D. R. Rowley, RUNX1 is essential for mesenchymal stem cell proliferation and myofibroblast differentiation. *Proc. Natl. Acad. Sci. U.S.A.* **111**, 16389–16394 (2014).
  38. A. Mezheyeuski, U. Segersten, L. W. Leiss, P. U. Malmström, J. Hatina, A. Östman, C. Strell, Fibroblasts in urothelial bladder cancer define stroma phenotypes that are associated with clinical outcome. *Sci. Rep.* **10**, 281 (2020).
  39. B. Hinz, D. Lagares, Evasion of apoptosis by myofibroblasts: A hallmark of fibrotic diseases. *Nat. Rev. Rheumatol.* **16**, 11–31 (2020).
  40. P. Bankhead, M. B. Loughrey, J. A. Fernández, Y. Dombrowski, D. G. McArt, P. D. Dunne, S. McQuaid, R. T. Gray, L. J. Murray, H. G. Coleman, J. A. James, M. Salto-Tellez, P. W. Hamilton, QuPath: Open source software for digital pathology image analysis. *Sci. Rep.* **7**, 16878 (2017).
  41. Q. Huang, L. Liu, D. Xiao, Z. Huang, W. Wang, K. Zhai, X. Fang, J. Kim, J. Liu, W. Liang, J. He, S. Bao, CD44<sup>+</sup> lung cancer stem cell-derived pericyte-like cells cause brain metastases through GPR124-enhanced trans-endothelial migration. *Cancer Cell* **41**, 1621–1636.e8 (2023).
  42. K. S. Chan, J. P. Volkmer, I. Weissman, Cancer stem cells in bladder cancer: A revisited and evolving concept. *Curr. Opin. Urol.* **20**, 393–397 (2010).
  43. Y. Fujita, M. Kitagawa, S. Nakamura, K. Azuma, G. Ishii, M. Higashi, H. Kishi, T. Hiwasa, K. Koda, N. Nakajima, K. Harigaya, CD44 signaling through focal adhesion kinase and its anti-apoptotic effect. *FEBS Lett.* **528**, 101–108 (2002).
  44. K. S. Chan, I. Espinosa, M. Chao, D. Wong, L. Ailles, M. Diehn, H. Gill, J. Presti Jr., H. Y. Chang, M. van de Rijn, L. Shortliffe, I. L. Weissman, Identification, molecular characterization, clinical prognosis, and therapeutic targeting of human bladder tumor-initiating cells. *Proc. Natl. Acad. Sci. U.S.A.* **106**, 14016–14021 (2009).
  45. C. M. Tilsed, S. A. Fisher, A. K. Nowak, R. A. Lake, W. J. Lesterhuis, Cancer chemotherapy: Insights into cellular and tumor microenvironmental mechanisms of action. *Front. Oncol.* **12**, 960317 (2022).
  46. B. Wiernicki, S. Maschalidi, J. Pinney, S. Adjemian, T. Vanden Berghe, K. S. Ravichandran, P. Vandenabeele, Cancer cells dying from ferroptosis impede dendritic cell-mediated anti-tumor immunity. *Nat. Commun.* **13**, 3676 (2022).
  47. R. Kim, A. Hashimoto, N. Markosyan, V. A. Tyurin, Y. Y. Tyurina, G. Kar, S. Fu, M. Sehgal, L. Garcia-Gerique, A. Kossenkova, B. A. Gebregziabher, J. W. Tobias, K. Hicks, R. A. Halpin, N. Cvetesic, H. Deng, L. Donthireddy, A. Greenberg, B. Nam, R. H. Vonderheide, Y. Nefedova, V. E. Kagan, D. I. Gabrilovich, Ferroptosis of tumour neutrophils causes immune suppression in cancer. *Nature* **612**, 338–346 (2022).
  48. G. Sollberger, G. E. Strittmatter, M. Garstkiewicz, J. Sand, H. D. Beer, Caspase-1: The inflammasome and beyond. *Innate Immun.* **20**, 115–125 (2014).
  49. M. D. Galsky, X. Guan, D. Rishipathak, A. S. Rapaport, H. M. Shehata, R. Banchemareau, K. Yuen, E. Varfolomeev, R. Hu, C.-J. Han, H. Li, Y. Liang, D. Vucic, L. Wang, J. Zhu, H. Yu, R. H. Herbst, E. Hajaj, E. Kiner, A. Bamias, M. De Santis, I. D. Davis, J. A. Arranz, E. Kikuchi, S. Bernhard, P. Williams, C. Lee, I. Mellman, S. Sanjabi, R. Johnston, P. C. Black, E. Grande, S. Mariathasan, Immunomodulatory effects and improved outcomes with cisplatin-versus carboplatin-based chemotherapy plus atezolizumab in urothelial cancer. *Cell Rep. Med.* **5**, 101393 (2024).
  50. M. Y. Teo, R. M. Bambury, E. C. Zabor, E. Jordan, H. Al-Ahmadie, M. E. Boyd, N. Bouvier, S. A. Mullane, E. K. Cha, N. Roper, I. Ostrovskaya, D. M. Hyman, B. H. Bochner, M. E. Arcila, D. B. Solit, M. F. Berger, D. F. Bajorin, J. Bellmunt, G. Iyer, J. E. Rosenberg, DNA damage response and repair gene alterations are associated with improved survival in patients with platinum-treated advanced urothelial carcinoma. *Clin. Cancer Res.* **23**, 3610–3618 (2017).
  51. A. Gil-Jimenez, J. van Dorp, A. Contreras-Sanz, K. van der Vos, D. J. Vis, L. Braaf, A. Broeks, R. Kerkhoven, K. E. M. van Kessel, M. J. Ribal, A. Alcaraz, L. F. A. Wessels, R. Seiler, J. L. Wright, L. Mengual, J. Boormans, B. W. G. van Rhijn, P. C. Black, M. S. van der Heijden, Assessment of predictive genomic biomarkers for response to cisplatin-based neoadjuvant chemotherapy in bladder cancer. *Eur. Urol.* **83**, 313–317 (2023).
  52. E. R. Plimack, C. Tangen, M. Plets, R. Kokate, J. Xiu, C. Nabhan, E. A. Ross, E. Grundy, W. Choi, C. P. N. Dinney, I. C. Lee, M. Fong, M. Lucia, S. S. Daneshmand, D. Theodorescu, A. Goldkorn, S. P. Lerner, T. W. Flaig, D. J. McConkey, Correlative analysis of ATM, RB1, ERCC2, and FANCC mutations and pathologic complete response after neoadjuvant

chemotherapy in patients with muscle-invasive bladder cancer: Results from the SWOG S1314 trial. *Eur. Urol.* **86**, 297–300 (2024).

53. Z. Zhang, Y. Zhang, S. Xia, Q. Kong, S. Li, X. Liu, C. Junqueira, K. F. Meza-Sosa, T. M. Y. Mok, J. Ansara, S. Sengupta, Y. Yao, H. Wu, J. Lieberman, Gasdermin E suppresses tumour growth by activating anti-tumour immunity. *Nature* **579**, 415–420 (2020).
54. Y. C. Lee, A. V. Kurtova, J. Xiao, F. Nikolos, K. Hayashi, Z. Tramel, A. Jain, F. Chen, M. Chokshi, C. Lee, G. Bao, X. Zhang, J. Shen, Q. Mo, S. Y. Jung, D. Rowley, K. S. Chan, Collagen-rich airway smooth muscle cells are a metastatic niche for tumor colonization in the lung. *Nat. Commun.* **10**, 2131 (2019).

#### Acknowledgments

**Funding:** We thank the National Cancer Institute (NCI) and Cancer Prevention and Research Institute of Texas (CPRIT) for the financial support to this study. This project is supported by R01CA175397 (K.S.C.), R01CA175397-S (K.S.C.), U54CA274375 (K.S.C.), R01CA255609 (K.S.C.), and CPRIT- RR230010 (K.S.C.), F31CA247257 (K.H.), and F31CA278582 (M.E.A.). This work utilized the

Houston Methodist Neal Cancer Center Spatial Omics Core. The Core was funded by Cancer Prevention and Research Institute of Texas (CPRIT: RR230010). **Author contributions:** Conceptualization: H.G. and K.S.C. Methodology: H.G., S.Q.R.W., E.S., Y.-C.L., K.H., M.E.A., A.K., and F.N. Investigation: H.G., S.Q.R.W., E.S., and K.H. Visualization: H.G., Y.H.H., M.K., Q.M., and X.P.H. Funding acquisition: K.S.C., K.H., and M.E.A. Clinical resources: Z.Z., S.S., R.S., and Z.M. Project administration: K.S.C. Supervision: H.G. and K.S.C. Writing—original draft: H.G. Writing—review and editing: S.Q.R.W., E.S., M.E.A., and K.S.C. **Competing interests:** The authors declare that they have no competing interests. **Data and materials availability:** All data needed to evaluate the conclusions in the paper are present in the paper and/or the Supplementary Materials.

Submitted 24 October 2024

Accepted 7 May 2025

Published 11 June 2025

10.1126/sciadv.adt8697